On the Shell Structure of Nuclear Bubbles [*]

Klaus Dietrich and Krzysztof Pomorski [†]
Technische Universität München, Garching, Germany

February 9, 2008

Abstract

We investigate the shell structure of spherical nuclear bubbles in simple phenomenological shell model potentials. The bunching is produced by the energy gaps between single-particle states with a different number of radial nodes. The shell correction energies for doubly magic bubbles may be as large as –40 MeV and probably imply a very long lifetime against spontaneous fission. β-stability occurs for ratios of the neutron number N to the proton number Z which differ markable from the β-stability valley of ordinary compact nuclei. The α–decay probability is shown to be very small for proton rich bubbles with a moderately large outer radius. Metastable islands of nuclear bubbles are shown to exist for nucleon in the range A=450–3000.

1   Introduction

The idea that stable or metastable nuclear bubbles might exist is rather old. Already in 1946 Wilson [1] has written about spherical bubble nuclei. J.A. Wheeler [2], in his famous notebook, mention the possibility that nuclei with different topology might exist. In 1967, P.J. Siemens and H.A. Bethe [3] studied the energy of strongly deformed spheroidal nuclei and of spherical bubble nuclei using a liquid drop model (LDM). They looked at nuclei in the region of the then expected superheavy nuclei but did not investigate the stability of the spherical bubbles with respect to deformations. F. Wong [4] was the first to perform detailed studies: Within the pure LDM he showed that for a fissibility parameter $X_0 > 2$ spherical nuclear bubbles have a lower energy than compact spherical nuclei but are not stable against fission. He then investigated the shell correction energy for toroidal and spherical bubble nuclei on the basis of a harmonic oscillator potential using the Strutinsky's method. In the study of the shell correction energy, he restricted his attention to known β–stable nuclei and found spherical bubbles with a very small inner

---

[†]On leave on absence from University M.C.S. in Lublin

radius as lowest energy configurations for certain doubly– magic known nuclei (^{138}Ce, ^{200}Hg).

More recently, L. Moretto et al. [5] investigated the effect of an ideal dilute classical gas of nucleons at finite temperature inside the bubble and claimed that the pressure exerted by this gas on the layer of nuclear matter could stabilize spherical bubbles against deformation. As the authors pointed out, this mechanism may also be of relevance for the existence of "mesoscopic bubbles".

In what follows we investigate the effects of the shell structure for spherical bubbles in a large range of neutron (N) and proton (Z) numbers considerably extending them beyond the known nuclear species. The present paper is an extension of our study presented in Ref. [6]. We use phenomenological shell model potentials and apply the Strutinsky method to evaluate the shell correction energy δE_{shell}. The motivation of this work is to find the magic neutron and proton numbers and to obtain an estimate of the magnitude of the shell energy. This simple approach is expected to be sufficiently realistic to establish the importance of shell effects in nuclear bubbles and to lead to a first assessment of the stability of such systems.

Surely, a reliable investigation of the existence of nuclear bubbles with an appreciable life-time versus fission and other decay channels requires careful and technically difficult Hartree-Fock (HF) or Hartree-Bogoliubov (HB) calculations. Indications that bubble solutions may exist have indeed already been found recently in HB-calculations with Gogny interactions [7] and some time ago [8] in HF-calculations based on the Skyrme interaction.

2 Theory

As in the original shell model of M. Göppert-Mayer and J. H. D. Jensen [9], we investigate the shell structure in the two limiting cases of a square well with infinite walls, on the one hand, and an oscillator potential, on the other.

In order to incorporate the case that the interior of the bubble is not entirely empty but filled by an internal halo of nucleons, we also investigate the effect of replacing the above mentioned single particle potentials by a constant potential of (small) finite depth V_2 for radial coordinates smaller than the inner radius (R_2) of the bubble.

The spin-orbit potential for a bubble nucleus is smaller than for an ordinary compact nucleus because the contributions arising from the inner and outer surface have a different sign. Therefore, we treated the spin-orbit potential in perturbation theory.

2.1 Eigenfunctions and eigenenergies of the spin-independent potentials

In the coupled representation which will turn out to be useful for the perturbative treatment of the spin–orbit potential, the eigenstates of the unperturbed Hamiltonian

$$\widehat{H}_0 = -\frac{\hbar^2}{2M}\Delta + V(r) \tag{2.1}$$

have the form

$$\psi_{nljm}(r,\theta,\phi) = \varphi_{nl}(r)\mathcal{Y}_{ljm}(\vartheta,\varphi) \tag{2.2}$$

$$\mathcal{Y}_{ljm} := \sum_{m_l,m_s} \langle lm_l\frac{1}{2}m_s|l\frac{1}{2}jm\rangle \, Y_{lm_l}(\theta,\phi)\chi_{m_s} \tag{2.3}$$

Here, $V(r)$ is a phenomenological spherically symmetric shell model potential. The quantities appearing in (2.3) have an obvious meaning. The radial wave functions $\varphi_{nl}(r)$ are normalized eigenfunctions of the radial Schrödinger equation

$$-\frac{\hbar^2}{2M}\left(\frac{\partial^2}{\partial r^2} + \frac{2}{r}\frac{\partial}{\partial r} - \frac{l(l+1)}{r^2}\right)\varphi_{nl} + (V(r)-\varepsilon_{nl})\,\varphi_{nl}(r) = 0\,, \tag{2.4}$$

which have to satisfy the boundary conditions

$$\varphi_{nl}(0) = 0 \qquad \text{for all} \quad l \neq 0; \quad \lim_{r\to 0}(r\varphi_{n0}(r)) = 0 \ , \tag{2.5.1}$$

$$\varphi_{nl}(\infty) = 0 \qquad \text{for all} \quad l \qquad\qquad . \tag{2.5.2}$$

The eigenvalues ε_{nl} and eigenfunctions $\varphi_{nl}(r)$ depend on the orbital angular momentum l and on the number of radial nodes. Not counting the zeros at $r = 0, \infty$, the number of radial nodes is given by $(n-1)$ where $n = 1, 2, \ldots$.

i) In the case of the infinite square-well

$$V(r) = \begin{cases} -V_0 & \text{for} \quad R_2 < r < R_1 \\ +\infty & \text{otherwise} \end{cases} \tag{2.6}$$

the boundary conditions (2.5) are replaced by

$$\varphi_{nl}(R_2) = \varphi_{nl}(R_1) = 0\,. \tag{2.7}$$

A finite well depth V_0 (= 50 MeV) is introduced for later convenience (see Eq. (2.11)). It has no influence on the shell correction energy. The eigenstates $\varphi_{nl}(r)$ are linear combinations of a spherical Bessel function $j_l(\alpha r)$ and a spherical Neumann function $y_l(\alpha r)$ (for "spherical Bessel function of the first and second kind", see Ref. [10])

$$\varphi_{nl}(r) = N_{nl}[j_l(\alpha r) + b_{nl}\, y_l(\alpha r)]\,. \tag{2.8}$$

The parameter α is defined by

$$\alpha = \sqrt{\frac{2M(\varepsilon_{nl} + V_0)}{\hbar^2}} \tag{2.9}$$

and the normalization constants N_{nl} are to be determined by the condition

$$\int dr \, r^2 |\varphi_{nl}(r)|^2 = 1 . \tag{2.10}$$

The two parameters ε_{nl} and b_{nl} are obtained by satisfying numerically the boundary conditions (2.7).

ii) In order to describe a finite density in the interior $(r < R_2)$ of the bubble, we consider the slightly more complicated potential

$$V(r) = \begin{cases} -V_2 & \text{for} \quad 0 \leq r < R_2 \\ -V_0 & \text{for} \quad R_2 < r < R_1 \\ +\infty & \text{for} \quad r > R_1 \end{cases} , \tag{2.11}$$

where the depth parameter $V_2 \, (> 0)$ in the interior region is substantially smaller than $V_0 \, (> 0)$. As a rough estimate one may choose the ratio V_2/V_0 to be equal to the ratio $\rho_{n(p)}^{(2)} / \mathring{\rho}_{n(p)}$ of the average density $\rho_{n(p)}^{(2)}$ of neutrons (protons) in the region $r < R_2$ to the uniform LD density $\mathring{\rho}_{n(p)}$ of neutrons (protons) in the region $R_2 < r < R_1$. The radial functions $\varphi_{nl}(r)$ and the eigenenergies $\mathring{\varepsilon}_{nl}$ which correspond to the infinite square well with internal step (2.11) are given in Appendix A1.

iii) As an opposite extreme to the one of the infinite square well we consider a harmonic oscillator with a finite internal step:

$$V(r) = \begin{cases} -V_2 & \text{for} \quad 0 \leq r < R_2 \quad (\text{region II}) \\ -V_0 + \frac{M\omega^2}{2}(r - \bar{R})^2 & \text{for} \quad r > R_2 \quad (\text{region I}) \end{cases} , \tag{2.12}$$

where

$$\bar{R} := \frac{1}{2}(R_1 + R_2) . \tag{2.13}$$

In Appendix A2 we exhibit the mathematical form of the radial eigenfunctions $\varphi_{nl}(r)$ for the potential (2.12) and discuss the numerical methods which may serve to obtain them.

The WKB method is known to yield the eigenvalues of simple nuclear potential models rather well we have therefore applied it in our case.

The upper (b) and lower (a) turning points for a particle of energy ε and orbital angular momentum l in the potential (2.12) are given as the real solutions of the equation

$$\varepsilon = \frac{\hbar^2 l(l+1)}{2Ma^2} + V(a) = \frac{\hbar^2 l(l+1)}{2Mb^2} + V(b) . \tag{2.14}$$

As the analytic roots of this quartic equations are complicated, it is more convenient to solve (2.14) numerically. The WKB-eigenvalues ε_{nl} are defined as the solutions of the equation [11]

$$\sqrt{2M} \int_a^b dr \sqrt{\varepsilon - V(r) - \frac{\hbar^2 l(l+1)}{2Mr^2}} = \left(n + \frac{1}{2}\right) \hbar\pi . \tag{2.15}$$

Here again an analytical integration is possible but impracticable whereas the numerical integration can be easily performed.

So far, we neglected the average Coulomb potential $V_{\mathrm{Cb}}(r)$ acting on the protons

$$V_{\mathrm{Cb}}(r) = e_0 \int d^3 r' \frac{\rho^{(p)}(\vec{r'})}{|\vec{r} - \vec{r'}|} . \tag{2.16}$$

If one replaces the density distribution $\rho^{(p)}(\vec{r})$ of the protons by a uniform distribution in the layer between the inner and outer LD-radius

$$\rho^{(p)}(\vec{r}) = \Theta_0(r - R_2)\Theta_0(R_1 - r)\overset{\circ}{\rho}_p , \tag{2.17}$$

$$\overset{\circ}{\rho}_p = \frac{3Ze_0}{4\pi(R_1^3 - R_2^3)} , \tag{2.18}$$

the Coulomb potential $V_{\mathrm{Cb}}(r)$ has the form

$$\begin{aligned} V_{\mathrm{Cb}}(r) &= \tfrac{4\pi}{3} e_0 \overset{\circ}{\rho}_p \left\{ \theta_0(R_2 - r)\tfrac{3(R_1^2 - R_2^2)}{2} + \theta_0(r - R_1) \cdot \tfrac{(R_1^3 - R_2^3)}{r} \right. \\ &\quad \left. + \theta_0(r - R_2)\theta_0(R_1 - r)\left(\tfrac{3R_1^2}{2} - \tfrac{R_2^3}{r} - \tfrac{r^2}{2}\right) \right\} . \end{aligned} \tag{2.19}$$

If one wishes to take this potential into account, the potential $V(r)$ must be replaced by $[V(r) + V_{\mathrm{Cb}}(r)]$ whenever it acts on protons.

We draw attention to the well-known result that a proton in the interior of the bubble $(r < R_2)$ feels a constant Coulomb potential. This means that only the repulsive Coulomb force between protons in the interior region disfavours the formation of an internal proton distribution as compared to the formation of an internal neutron distribution.

At this point, we would like to make the following remark: The shell correction energy δE_{shell} is invariant with respect to a constant shift of all the eigenvalues of a given sort of particles. The shifts can be different for neutrons and protons. This is the reason why we may identify the nuclear part $V(r)$ for n and p as long as we neglect the Coulomb potential and assume that the other parameters of the potential (radius parameter $R_{1,2}$, frequency ω) are the same for n and p. This simple assumption turned out to be empirically very successful for the Nilsson potential. Therefore, we adopt it too, realizing at the same time that it may be insufficiently accurate for cases of very exotic nuclear compositions.

The effect of a finite potential $V_2 \neq 0$ in the interior region $r < R_2$ is qualitatively the same for the two potentials (2.11) and (2.12). Therefore, we studied the effect of a

finite value of V_2 only for the infinite square well. In all calculations with the harmonic oscillator potential (2.12) the parameter V_2 was chosen to be 0 :

$$V(r) = -V_0 + \frac{M\omega^2}{2}(r - \bar{R})^2 \quad \text{for} \quad r \geq 0 \; . \tag{2.20}$$

Furthermore, we determined the eigenvalues ε_{nl} corresponding to the potential (2.20) from the WKB approximation and the radial s.p. densities

$$\rho_{nl}(r) = \varphi_{nl}^2(r)$$

from the Thomas-Fermi model. The details of this procedure are presented in Appendix A3.

We still have to state how the "shape parameters" of the shell model potentials are to be chosen: Since we use the Strutinsky method representing the total binding energy of the nucleus as a sum of the liquid drop (LD) energy E_{LD} and the shell correction energy $\delta E_{\mathrm{shell}}$, the shape parameters of the shell model potential must be chosen in accordance with the ones of the liquid drop. When calculating the energy as a function of the nuclear shape, the multipole moments (of low order) calculated with the shell-model wavefunction must agree with the ones calculated with the LD-density. For the case of spherical bubble nuclei, the MS deviation from the central sphere of radius $\bar{R}$ must be the same when calculated with the shell-model wave function and with the LD-density

$$\langle (r - \bar{R})^2 \rangle_{\mathrm{SM}} = \langle (r - \bar{R})^2 \rangle_{\mathrm{LD}} \; , \tag{2.21}$$

where

$$\bar{R} := \frac{1}{2}(R_1 + R_2) \; . \tag{2.21'}$$

We restrict our consideration to bubble nuclei with a negligible nuclear density inside of the smaller radius R_2 of the LD-distribution. This means that we only consider the cases of the infinite square well and of the shifted oscillator without an internal step (see Eq. (2.20)).

For the shifted oscillator, the condition (2.21) may serve to fix the frequency ω. For the square well potential it is physically reasonable to choose the potential walls at a slightly larger spacing than the difference of the LD-radii

$$\tilde{R}_1 = R_1 + \Delta R \; , \tag{2.22}$$

$$\tilde{R}_2 = R_2 + \Delta R \; . \tag{2.22'}$$

The condition (2.21) may then serve to determine the parameter ΔR. One could modify these constraints slightly. So the shift (2.22) of the inner and outer radius of the potential with respect to the ones of the liquid drop need not be equal and the reference radius $\bar{R}$ (see (2.21')) might be chosen differently. We believe that the simple choices we made are reasonable given the fact that the Strutinsky method itself is of limited accuracy.

The MS-radius calculated within the LDM is given by

$$\langle (r - \bar{R})^2 \rangle_{\mathrm{LD}} = \frac{\frac{1}{10}(R_1{}^5 - R_2{}^5) + \frac{1}{4}(-R_1{}^4 R_2 + R_1{}^3 R_2{}^2 - R_1{}^2 R_2{}^3 + R_1 R_2{}^4)}{(R_1{}^3 - R_2{}^3)} \, . \qquad (2.23)$$

The MS-radius $\langle (r - \bar{R})^2 \rangle_{\mathrm{SM}}$ in the shell model is approximately calculated in the Thomas-Fermi approximation (see Appendix A3):

$$\begin{aligned} \langle (r - \bar{R})^2 \rangle_{\mathrm{SM}} \quad &\approx \frac{2}{h^3} \int d^3 r \int d^3 p \, (r - \bar{R})^2 \left\{ \theta_0 \left[\varepsilon_F^n - \frac{p^2}{2M} - V(r) \right] + \right. \\ &\left. + \theta_0 \left[\varepsilon_F^p - \frac{p^2}{2M} - V(r) - V_{\mathrm{Cb}}(r) \right] \right\} . \end{aligned} \qquad (2.24)$$

The Fermi energies ε_F^n, ε_F^p for the neutrons and protons are determined by the number N of neutrons and Z of protons

$$\begin{aligned} N \quad &= \frac{2}{h^3} \int d^3 r \int d^3 p \, \theta_0 \left[\varepsilon_F^n - \frac{p^2}{2M} - V(r) \right] \\ &= \frac{32\pi^2 (2M)^{3/2}}{h^3} \int_{r_2^n}^{r_1^n} [\varepsilon_F^n - V(r)]^{3/2} \, , \end{aligned} \qquad (2.25.1)$$

$$\begin{aligned} Z \quad &= \frac{2}{h^3} \int d^3 r \int d^3 p \, \theta_0 \left[\varepsilon_F^p - \frac{p^2}{2M} - V(r) - V_{\mathrm{Cb}}(r) \right] \\ &= \frac{32\pi^2 (2M)^{3/2}}{h^3} \int_{r_2^p}^{r_1^p} [\varepsilon_F^p - V(r) - V_{\mathrm{Cb}}(r)]^{3/2} \, . \end{aligned} \qquad (2.25.2)$$

All integrations but one can be trivially done and we obtain

$$\langle (r - R)^2 \rangle_{\mathrm{SM}} \approx \frac{32\pi^2 (2M)^{\frac{3}{2}}}{h^3} (J_n + J_p) \, , \qquad (2.26.1)$$

$$J_n := \int_{r_2^n}^{r_1} dr \, r^2 (r - \bar{R})^2 \left[\varepsilon_F^n - V(r) \right]^{\frac{3}{2}} \, , \qquad (2.26.2)$$

$$J_p := \int_{r_2^p}^{r_1^p} dr \, r^2 (r - \bar{R})^2 \left[\varepsilon_F^p - V(r) - V_{\mathrm{Cb}}(r) \right]^{\frac{3}{2}} \, . \qquad (2.26.3)$$

The limits of the integrals are the (lower and upper) classical turning points of a particle with energy ε_F in the potential $V(r)$

$$V(r_2^n) = V(r_1^n) = \varepsilon_F^n \qquad (2.27.1)$$

$$V(r_2^p) + V_{Cb}(r_2^p) = V(r_1^p) + V_{Cb}(r_1^p) = \varepsilon_F^p \, . \qquad (2.27.2)$$

We neglect the Coulomb potential in the numerical calculations.

2.2 Spin-orbit potential

In the conventionally used Skyrme interactions, the effective spin-orbit interaction between two nucleons has the form

$$v_{\mathrm{SO}} := i \, W_o (\vec{\sigma}_1 + \vec{\sigma}_2) \widehat{\vec{k}} \times \delta(\vec{r}_1 - \vec{r}_2) \widehat{\vec{k}} \, , \qquad (2.28)$$

where $W_o \approx 120$ MeV fm^5 and

$$\widehat{\vec{k}} := \frac{1}{2i}(\vec{\nabla}_1 - \vec{\nabla}_2) . \tag{2.28'}$$

This interaction leads to the following one-body spin-orbit potential [12]

$$\widehat{V}_{SO} = \vec{W}(\vec{r}) \frac{1}{i}(\vec{\nabla} \times \vec{\sigma}) , \tag{2.29}$$

$$\vec{W}(\vec{r}) := \frac{3W_o}{4} \vec{\nabla}\rho(\vec{r}) . \tag{2.29'}$$

Here $\rho(\vec{r})$ is the sum of the density distribution of neutrons ($\rho_n(\vec{r})$) and protons ($\rho_p(\vec{r})$). Recently, Reinhard and Flocard [13] generalized the ansatz (2.28) for the spin-orbit interaction in such a way that the vector $\vec{W}(\vec{r})$ (2.29') takes the more general form

$$\vec{W}_{n(p)}(\vec{r}) = b_4 \vec{\nabla}\rho(\vec{r}) + b_4' \vec{\nabla}\rho_{n(p)}(\vec{r}) \tag{2.30}$$

for neutrons and protons, resp. Here, b_4, b_4' are parameters in the notation of Ref. [13] which have the values $b_4 = b_4, = 62.130$ MeV fm^5 for the Skyrme interaction SkI1. This choice corresponds roughly to the value of the parameter $W_o \approx 120$ MeV fm^5, if the numbers of neutrons (N) and protons (Z) are equal. For unequal numbers of n and p, the form (2.30) yields are more flexible form of the spin-orbit potential. With the choice $b_4 = b_4' = 62.130$ MeV fm^5 one reproduces the empirical values of the isomer shifts across magic shell closures [13].

For spherically symmetric density distributions the spin-orbit potential $\widehat{V}_{SO}$ takes the form

$$\widehat{V}_{SO}^{n(p)} = \frac{2}{r}\left(b_4\frac{\partial\rho(r)}{\partial r} + b_4'\frac{\partial\rho_{n(p)}(r)}{\partial r}\right)\widehat{\vec{l}}\cdot\widehat{\vec{s}}, \tag{2.31}$$

where $\widehat{\vec{s}}$ is the dimesionless spin-operator and $\widehat{\vec{l}}$ is given by

$$\widehat{\vec{l}} := \vec{r} \times \frac{1}{i}\vec{\nabla} . \tag{2.31'}$$

For symmetric spherical nuclei

$$\rho_n(r) = \rho_p(r) = \frac{1}{2}\rho(r) \tag{2.32}$$

one obtains the still simpler form

$$V_{SO}^{(n)} = V_{SO}^{(p)} = \widehat{V}_{SO} = \frac{2}{r}(b_4 + \frac{1}{2}b_4')\frac{\partial\rho(r)}{\partial r}\widehat{\vec{l}}\cdot\widehat{\vec{s}}, \tag{2.33}$$

which is equivalent to the conventional isospin independent form of the spin-orbit potential of a spherical nucleus (see Eqn. (5.103) in Ref. [11])

$$\widehat{V}_{SO} = \frac{3}{2}W_o\frac{1}{r}\frac{\partial\rho(r)}{\partial r}\widehat{\vec{l}}\cdot\widehat{\vec{s}} . \tag{2.33'}$$

8

So far, our calculation of the spin-orbit coupling is based on the isoscalar form (2.33') of the spin-orbit potential. Furthermore, we used phenomenological forms for the densities $\rho_{n(p)}(r)$ rather than the "selfconsistent" densities which could be obtained from the single-particle functions. The following density distributions were used

$$\rho_{n(p)}(r) = \rho_o^{n(p)} \left\{ \frac{1}{1 + e^{\frac{r - R_1}{a}}} - \frac{1}{1 + e^{\frac{r - R_2}{a}}} \right\} \qquad (2.34.1)$$

$$\rho_{n(p)}(r) = \rho_o^{n(p)} \left\{ \left(1 + e^{\frac{r - R_1}{a}}\right) \left(1 + e^{\frac{R_2 - r}{a}}\right) \right\}^{-1} \qquad (2.34.2)$$

$$\rho_{n(p)}(r) = \rho_o^{n(p)} \theta_o(r - R_2) \theta_o(R_1 - r)(1 - \kappa(r - \bar{R})^2) . \qquad (2.34.3)$$

where $\bar{R} = \frac{1}{2}(R_1 + R_2)$. The parameters $\rho_o^{n(p)}$ are determined by number conservation

$$N(Z) = \int d^3r \, \rho_{n(p)}(r) . \qquad (2.35)$$

The results obtained from the different forms of $\rho_{n(p)}(r)$ are very similar. The parameter κ in (2.34.3) is chosen in such a way that the density at $r = R_{1(2)}$ is equal $\rho_0^{n(p)}/2$:

$$\kappa = \frac{2}{(R_1 - R_2)^2} . \qquad (2.36)$$

The parabolic choice (2.34.3) of the density yields a particularly simple form of the spin-orbit potential:

$$\widehat{V}_{\text{SO}}^{n(p)} = -\frac{12 W_o \, \rho_o^{n(p)}}{(R_1 - R_2)^2} \left(\frac{r - \bar{R}}{r}\right) \widehat{\vec{l}} \cdot \widehat{\vec{s}}. \qquad (2.37)$$

Using the unperturbed eigenstates in the coupled representation (2.2), we obtain the shift $\Delta\varepsilon_{nlj}$ of unperturbed eigenvalue $\overset{\circ}{\varepsilon}_{nl}$ due to the spin-orbit potential

$$\Delta\varepsilon_{nlj} = \frac{3}{2} W_o \cdot 4\pi \int_0^\infty dr \, r \frac{\partial \rho(r)}{\partial r} \overset{\circ}{\rho}_{nl}(r) \cdot \left[j(j+1) - l(l+1) - \frac{3}{4} \right] \qquad (2.38)$$

$$\varepsilon_{nlj} = \overset{\circ}{\varepsilon}_{nl} + \Delta\varepsilon_{nlj} . \qquad (2.39)$$

In Eq. (2.38), the function $\overset{\circ}{\rho}_{nl}(r)$ is the unperturbed single particle density

$$\overset{\circ}{\rho}_{nl} = \int d\Omega \, \psi_{nljm}^+ \psi_{nljm} = \varphi_{nl}^\star(r) \varphi_{nl}(r) . \qquad (2.40)$$

The total angular momentum j in (2.38) can assume one of the two values $j = |l \pm \frac{1}{2}|$. The approximate calculation of $\overset{\circ}{\rho}_{nl}(r)$ is described in Appendix A3.

3 Results

3.1 Bubble nuclei in the LDM

As we have stated already in the introduction, C.Y. Wong [4] investigated the stability of bubble nuclei within the liquid drop (LD) model. Also the role of the shell effects has been first discussed in Ref. [4]. The result was that while for large enough mass (A) and charge numbers (Z) spherical bubble configurations do have a lower energy than the compact spherical ones, the energy can still be lowered by deforming the bubble. This means that no barrier protects the spherical bubble nuclei from undergoing fission.

It is useful to represent these results in a simple form. We denote the inner and outer radius of the spherical bubble nucleus by R_2 and R_1, resp., and the radius of the compact spherical nucleus of the same mass number by R_0. We retain the conventional basic assumptions of the LDM that the charge is uniformly distributed over the nuclear matter and that the nuclear density is constant inside the matter distribution dropping abruptly to zero at the surface.

The difference ΔE_{LD} between the energy of the bubble configuration with radii $R_{1,2}$ and the energy of a compact spherical nucleus of radius R_0 is given by

$$\Delta E_{\mathrm{LD}} = 4\pi\sigma(R_1^2 + R_2^2 - R_0^2) + E_{\mathrm{Cb}}(R_1, R_2) - E_{\mathrm{Cb}}(R_0) \,, \tag{3.1}$$

where σ is the surface tension parameter.

The Coulomb energy $E_{\mathrm{Cb}}(R_1, R_2)$ of the spherical bubble nucleus is defined as a function of the proton density $\rho_p(r)$ and the Coulomb potential $V_{Cb}(r)$ by

$$E_{\mathrm{Cb}}(R_1, R_2) = \frac{1}{2} \int d^3r \, V_{Cb}(r)\rho_p(r) \,. \tag{3.2}$$

The LD–density $\rho_p(r)$ is represented by the simple formula (θ_0 = Heaviside function)

$$\rho_p(r) = \theta_0(R_1 - r)\theta_0(r - R_2) \, \overset{\circ}{\rho}_p \tag{3.2'}$$

and the corresponding Coulomb potential is given by Eq. (2.19). The Coulomb energy of the LD–bubble is then obtained in the form

$$E_{\mathrm{Cb}}(R_1, R_2) = \frac{8\pi^2 \, \overset{\circ}{\rho}_p^2}{3} \left[\frac{2}{5}R_1^5 + \frac{3}{5}R_2^5 - R_1^2 R_2^3\right] \tag{3.3}$$

$$\overset{\circ}{\rho}_p = \frac{3Ze_0}{4\pi R_0^3} \tag{3.3'}$$

The Coulomb energy $E_{\mathrm{Cb}}(R_0)$ of the homogeneously charged sphere is

$$E_{\mathrm{Cb}}(R_0) = \frac{3Z^2 e_0^2}{5R_0} \,, \tag{3.4}$$

The condition of volume conservation yields the relation

$$R_0^3 = R_1^3 - R_2^3. \tag{3.5}$$

It is easily seen that the energy difference ΔE_{LD} in units of the surface energy of the spherical compact nucleus $4\pi\sigma R_0^2$ can be written as

$$\mathcal{E} := \frac{\Delta E_{\mathrm{LD}}}{4\pi\sigma R_0^2} = v_1^2(v_2) + v_2^2 - 1 + 2X_0 \left[v_1^5(v_2) + \frac{3}{2}v_2^5 - \frac{5}{2}v_2^3 v_1^2(v_2) - 1 \right]. \tag{3.6}$$

v_1 and v_2 are the radii of the outer and inner surface in units of R_0, resp. They are related by:

$$v_1 = \frac{R_1}{R_0} = \left(1 + \frac{R_2^3}{R_0^3} \right)^{1/3} = (1 + v_2^3)^{1/3} \tag{3.7}$$

X_0 is the conventional fissility parameter defined by

$$X_0 = \frac{E_{\mathrm{Cb}}(R_0)}{2 \cdot 4\pi\sigma R_0^2} = \frac{3Z^2 e_0^2}{40\pi\sigma R_0^3} = \frac{(Z^2/A)}{(Z^2/A)_{\mathrm{crit}}}. \tag{3.8}$$

The dimensionless parameter $(Z^2/A)_{\mathrm{crit}}$ defined by the last Eq. (3.8)

$$(Z^2/A)_{\mathrm{crit}} = \frac{40\pi\sigma r_0^3}{3e_0^2} \tag{3.8'}$$

depends on the value of the surface tension constant σ and the radius parameter r_0. For $r_0 = 1, 2$ fm and $\sigma = 1.026$ MeV fm^{-2} one obtains $(Z^2/A)_{\mathrm{crit}} = 51.57$. We draw attention to the fact that the difference (in units of the surface energy $E_S = 4\pi\sigma R_0^2$) $\mathcal{E}$ between the energy of the bubble configuration and the energy of the compact sphere depends only on the fissility parameter X_0.

The condition of stationarity reads

$$\frac{\partial \mathcal{E}}{\partial v_2} = \frac{2v_2^2}{v_1(v_2)} + 2v_2 + 2X_0 \left[-\frac{5}{2}v_2^2 v_1^2(v_2) + \frac{15}{2}v_2^4 - \frac{5v_2^5}{v_1(v_2)} \right] = 0. \tag{3.9}$$

where $v_1(v_2)$ is defined be Eq. (3.7).

Beside the trivial solution $v_2 = 0$ (compact sphere), the equation (3.9) has 2 additional real solutions[1] if and only if $X_0 \geq 2.02$. We can write Eq. (3.9) in the form

$$X_0 = \frac{2}{5} \cdot \left[\frac{v_2 + v_1(v_2)}{v_2 + 3v_2^3(v_2 - v_1(v_2))} \right]. \tag{3.10}$$

The inverse $v_2(X_0)$ of (3.10) describes the values of v_2 which correspond to stationary values of the energy $\mathcal{E}$. The function is shown in Fig. 1. From this figure, one sees in an illustrative way that for given $X_0 > 2.02$ there are 2 real positive solutions $v_2(X_0)$. As is to be seen in Fig. 2, the smaller one ($v_2^<(X_0)$) corresponds to a maximum and the larger one ($v_2^>(X_0)$) to a minimum of the energy $\mathcal{E}$.

---

[1]Real solutions with still larger v_2 may exist but they are physically meaningless.

For small values of v_2 ($v_2^3 \ll 1$), the energy change $\mathcal{E}$ by bubble formation can be written approximately as

$$\mathcal{E} \approx v_2^2 + \frac{1}{3}(2 - 5X_0)v_2^3 + 3X_0 v_2^5 + O(v_2^6)\,. \tag{3.11}$$

This shows that the compact spherical LD ($v_2 = 0$) is always "locally" stable with respect to bubble formation independently of the value of X_0. In other words: If there is at all a bubble solution, then it is separated from the compact sphere by a barrier.

It is a curious result that the inner and outer radius of the bubble nucleus (measured in units of $R_0 = r_0 A^{1/3}$) depend only on the fissility parameter X_0. If the parameter $(Z^2/A)_{\mathrm{crit}}$ (see (3.8')) is independent on $(N - Z)$, a given value of the fissility parameter X_0 implies a given value of Z^2/A.

For $(Z^2/A)_{\mathrm{crit}}$=51.57, bubble solutions within the LDM are only obtained for

$$\frac{Z^2}{A} > 2.02 \times \left(\frac{Z^2}{A}\right)_{\mathrm{crit}} \approx 104\,. \tag{3.12}$$

Thus, for given nucleon number A, the charge must be larger than a minimal value for LD-bubble solutions to exist. From (3.12) we obtain $Z > 250$ for $A = 600$ and $Z > 353$ for $A = 1200$. The minimal proton density, necessary for LD-bubble solutions to exist, is thus the larger, the smaller the nucleon number A.

Let us restate clearly:*If we speak about the existence of a bubble in the LD theory, we only mean that a minimum of the LD-energy with respect to (volume-conserving) changes of the bubble radii exists. As we shall show later, and as it was shown by the author of Ref. [4], these spherical solutions are unstable against deformation of the bubble.*

Nevertheless, it is physically meaningful to study carefully the conditions for the existence of bubble solutions in the LDM, because whenever these solutions exist, the shell structure effects have a better chance to make the bubbles stable.

The Figs. 3–5 are designed to give a global view on the LD-properties of bubble nuclei. There results were obtained with the parameters of the liquid drop model taken from Ref. [15].

In Fig. 3, lines of constant fissility parameter

$$X := \frac{E_{\mathrm{Cb}}(R_1, R_2)}{8\pi\sigma(R_1^2 + R_2^2)} \tag{3.13}$$

are shown in the (N, Z)-plane. Each point corresponds to an existing bubble solution. We draw the reader's attention to the fact that the fissility parameter X defined in Eq. (3.13) differs from the fissility parameter X_0, which refers to a compact spherical nucleus of radius R_0. The two fissility parameters are related by

$$X = X_0 \frac{v_1^5 + \frac{3}{2}v_2^5 - \frac{5}{2}v_1^2 v_2^3}{v_1^2 + v_2^2} = X_0 \frac{\left(1 + \frac{3}{2}f^{5/3} - \frac{5}{2}f\right)}{(1 - f^{5/3} - f + f^{2/3})}\,, \tag{3.14}$$

12

where the parameter f is defined as the fraction of the empty volume to the total volume of the bubble

$$f = \left(\frac{R_2}{R_1}\right)^3 . \tag{3.15}$$

Contrary to X_0, the fissility parameter X depends on the two reduced radii of the bubble. It is a measure of the fissility of the spherical LD bubble. The larger the value of X the more rapid is the descent of the energy as a function of the deformation.

Each point on the contour lines shown in Fig. 3 corresponds to a bubble solution. The parallel straight lines represent isobars. As one moves on a given isobar towards nuclei with a larger proton density, the fissility parameter in general decreases, i.e. the LD-bubbles become less unstable versus fission. A peculiar feature is that the line of fissility $X=1.25$ is cut twice by the isobaric lines. This means that for given A there may exist two bubble solutions corresponding to the same fissility X but different charge numbers and different bubble radii. Of course, the 2 solutions belong to different binding energies in general.

Lines of equal binding energy gain ΔE_{LD} (see (3.1)) in the (N, Z)-plane are shown in Fig. 4. The parallel straight lines indicate again isobars. On the proton rich region of the figure for given A, the binding energy gains due to bubble formation are the larger, the larger the charge Z. This can be easily understood by the fact that the decrease of the repulsive Coulomb energy due to bubble formation is larger for larger charges. Certain equi-energy lines are cut twice by given isobars. This means that there are two isobaric nuclei (N_1, Z_1) and (N_2, Z_2) with bubble solutions corresponding to the same energy gain, but in general different bubble radii. Following the isobaric lines in the direction of larger binding energy, one can infer the type of β-decays to be expected. Curiously, on the p-rich side, β^+-decays would increase the binding energy even further. These considerations must of course be taken with a grain of salt, because the bubbles are in general not stable with regard to fission. Stability can only be produced by shell effects which complicate the topology of the equi-energy lines.

In Fig. 5 we display lines of equal hole parameter f in the (N, Z)-plane. Large f means that the interior hole represents a large part of the total bubble volume. It is seen that in general, as one increases the charge Z along an isobaric line, the hole fraction increases. Again there are pairs of isobaric nuclei (N_1, Z_1), (N_2, Z_2) with bubbles of the same shape at different neutron and proton numbers. The energies of such pairs are usually different.

In Fig. 6, we display lines of equal total binding energy per particle for LD-bubbles in the (N, Z)-plane. It is remarkably different from Fig. 4 where we showed lines of constant total binding energy gain due to bubble formation. As a general trend, the total LD-binding energy per particle tends to decrease as the proton number increases along an isobaric line. The largest binding energies per particle are seen to occur in the region 1000<N<1800 and 300<Z<400. It is also interesting to see an island of very small (absolute) binding energy per nucleon in the region of 400<N<600 and 380<Z<480. Again we observe pairs of isobars showing the same binding energy per particle.

Let us emphasize that the simple features of the Figs. 3–6 are due to the simplicity

of the LDM. As a macroscopic model it predicts a smooth dependence of all the physical properties on N and Z. The shell effects, which will be shown to prevent certain magic bubble nuclei from undergoing fission, will complicate the picture considerably. The shell structure will be seen to modify the smooth trends of the LDM profoundly, but only in certain localized regions of the (N, Z)-plane.

So far, we only considered spherical nuclei. A crucial question is whether the spherical bubbles are stable with respect to deformations of the inner (S_2) and outer (S_1) surface. Within the LD approximation, we have to study the energy difference

$$\Delta E_{\mathrm{LD}}(S_2, S_1) := E_{\mathrm{LD}}(S_2, S_1) - E_{\mathrm{LD}}(R_2, R_1)\,, \tag{3.16}$$

where $E_{\mathrm{LD}}(S_2, S_1)$ is the energy of a deformed LD bubble with the inner and outer surface S_2 and S_1, resp., and $E_{\mathrm{LD}}(R_2, R_1)$ is the LD-energy of the spherical bubble with radii R_2, R_1.

As the volume terms cancel again, we have

$$\begin{aligned}\Delta E_{\mathrm{LD}}(S_2, S_1) \;\; &= \sigma\left[S_2 + S_1 - 4\pi R_2^2 - 4\pi R_1^2\right]\\ &+ \left[\tfrac{1}{2}\int \frac{\rho_p(\vec{r}_1)\rho_p(\vec{r}_2)}{|\vec{r}_r-\vec{r}_2|}d^3r_1 d^3r_2 - E_{\mathrm{Cb}}(R_2, R_1)\right]\,,\end{aligned} \tag{3.17}$$

where $S_{2(1)}$ denote the magnitude of the deformed inner (outer) surface and $\rho_p(\vec{r})$ is the uniform charge distribution within the volume enclosed by S_2 and S_1. An investigation of ΔE_{LD} shows [4] that the spherical LD bubbles are not minima but saddle points in a multi-dimensional potential surface. In particular, the energy of a spherical LD bubble is lowered by quadrupole deformations.

In Fig. 21 we show the energy ΔE_{LD} as a function of the quadrupole deformation of the outer surface. The energy is seen to decrease for prolate as well as for oblate deformation of the bubble. It is also seen from this figure that constraints on the shape of the inner surface (for given deformation of the outer one) increase the energy substantially.

As is well-known, ordinary compact spherical liquid drops are unstable with respect to fission for fissility parameters $X_0 > 1$. This means that the formation of a bubble nucleus by a fusion of 2 nuclei, is complicated by the fact that only a tiny part of the reaction cross section is expected to contribute to the formation of a bubble.

3.2   The level spectrum

As explained in Sect. 2, we calculated the level spectrum for the shifted infinite square well and the shifted oscillator treating the $\vec{l}\vec{s}$-coupling in perturbation theory. We also studied the effects of a finite negative constant potential in the interior region for the case of the square well. This corresponds to the case of a bubble nucleus with a reduced but nonvanishing internal density.

In Fig. 7, we show the level spectrum for the shifted infinite square well as a function of the hole fraction f. A nice feature of the shifted infinite square well is that its eigenvalues scale with $A^{-2/3}$. We have used the unit $100/A^{2/3}$ MeV. Consequently, from the spectrum given in Fig. 7 one can infer the eigenvalues for arbitrary nucleon number A.

We use the conventional spectroscopic notation (nlj): $n = 1, 2, \ldots$ counts the eigenvalues for given l, j in rising order. Apart from s, p, d ($l = 0, 1, 2$) the angular momentum l is represented by the letters in alphabetical order ($f, g, h, \ldots \sim l = 3, 4, 5 \ldots$).

The following physical features of the spectrum should be noted: for $n = 1$, the single particle energies e_{nlj} decrease as a function of f, for $n > 2$, they increase as a function of f with a steepness which becomes drastically larger with n. The dependence on n is produced by the requirement of a vanishing wavefunction at the limits of the well. As f increases, the diameter $d \equiv R_1 - R_2$ diminishes and, consequently, the energy difference between successive radial modes increases.

The strong dependence of the difference between successive eigenvalues of the same orbital angular momentum l but different radial modes can be understood in the following simple approximation: If we replace the centrifugal term $\frac{l(l+1)\hbar^2}{2Mr^2}$ in the radial Schrödinger equation by its value at the center $\bar{R} = \frac{R_1 + R_2}{2}$ of the bubble layer, the eigenfunctions $u_{nl}(r)$ become trigonometric functions which are either "even" or "odd" with respect to the reflection $(r - \bar{R}) \to -(r - \bar{R})$. In this approximation the eigenenergies have the form ($n' = 0, 1, \ldots$)

$$\varepsilon_{nl} \approx \frac{\hbar^2 l(l+1)}{2M\bar{R}^2} + \frac{h^2}{8Md^2} \cdot \begin{cases} (2n'+1)^2 & \text{for even states} \\ (2n'+2)^2 & \text{for odd states} \end{cases} . \tag{3.15}$$

One can easily check that this relation explains qualitatively the behaviour of the eigenvalues as a function of the hole fraction f. We note that

$$d^2 = R_0^2 \frac{(1 - f^{1/3})^2}{(1 - f)^{2/3}} \tag{3.16.1}$$

$$\bar{R}^2 = \frac{R_0^2}{4} \frac{(1 + f^{1/3})^2}{(1 - f)^{2/3}} \tag{3.16.2}$$

and that the spectroscopic label n is related to n' by

$$\begin{array}{lll} n = 1 & \sim & n' = 0, \quad \text{even state} \\ n = 2 & \sim & n' = 0, \quad \text{odd state} \\ n = 3 & \sim & n' = 1, \quad \text{even state} \\ & a.s.o. & \end{array} \tag{3.17}$$

The gentle dependence of the energies with $n = 1$ as a function of f is due to the fact that in this case the increase of the second term in (3.15) is largely compensated by the decrease of the first term in (3.15).

Let us stress that the approximation (3.15) is crude and cannot replace the determination of the true unperturbed eigenvalues by a numerical solution of the Eqs. (2.7).

In Fig. 7 we plotted the energy levels including the spin-orbit interaction

$$e_\nu = e_{nlj} = \varepsilon_{nl} + \langle \psi_{nljm} | V_{\text{SO}} | \psi_{nljm} \rangle . \tag{3.18}$$

An unusual feature is that the levels with $j = l - \frac{1}{2}$ lie below the levels with $j = l + \frac{1}{2}$. Furthermore, the spin-orbit splitting, i.e. the energy difference $|e_{nll-\frac{1}{2}} - e_{nll+\frac{1}{2}}|$ is much

smaller than in the case of ordinary nuclei with the same l. The reason for both these phenomena is difference of the density distributions: Since the spin-orbit term depends on the gradient of the density (see Eq. (2.29'),(2.30)), its main contribution originates from the nuclear surface. The outer surface contributes with the same sign, but the inner with the opposite sign as compared to ordinary nuclei. For spherical bubble nuclei the spin-orbit potential can be written in the form (2.31). The factor $1/r$ in the expression weighs the inner surface more than the outer one so that the sign change becomes understandable. The infinite square well model is, of course, not realistic especially for bubble nuclei with a small value of f. In the case of bubbles with a small hole fraction, we cannot expect the hole to be empty. It will rather be filled with a reduced nucleon density and thus the change at the inner surface from the density in the layer to the reduced density in the hole region will be much smoother than in the case of the infinite square well. In this case, the contribution of the outer surface may become more important than the one of the inner surface in spite of the weight factor $1/r$ and thus the usual order of spin-orbit splitting ensues.

In the Fig. 8 we show the level scheme as a function of the parameter f for the shifted oscillator. The oscillator is more suitable than the infinite square well (i) for small f-values, where the inner region is expected to contain a reduced density of nucleons, and (ii) for bubbles with a thin layer, i.e. with a diameter d which becomes smaller than about 4 fm. As one can infer from (3.16.1) this happens for large values of f and at the same time not too large values of A. (Example: f=0.3 (0.4) yields d/R_0=0.37 (0.31) and consequently d=3.9 fm (3.3 fm) for A=700.) Contrary to the case of the infinite square well, there are also cases of "normal" order of the spin-orbit splitting (see for instance the pairs $\left(2i\frac{13}{2}, 2i\frac{11}{2}\right)$ and $\left(1k\frac{17}{2}, 1k\frac{15}{2}\right)$) for the harmonic oscillator potential.

The following general trends can be stated:

(i) For increasing hole fraction f, the contributions of the inner and outer surface region to the total spin-orbit term tend to become more equal. Since the two regions contribute with opposite sign, the spin-orbit splitting tends to decrease with increasing f. This is seen in Fig. 7 and 8, i.e. for both the potentials.

(ii) The centrifugal potential has the tendency of shifting the single particle density to larger values of f. For given hole fraction f, this effect increases with l and for given l, the effect decreases with f. This shift of the s.p. density towards larger values of r is expected to increase the contribution of the outer surface region as compared to the inner one as far as the spin-orbit term is concerned.

In fact one can observe in Fig. 8 that for large enough l and small f the "normal" spin-orbit splitting prevails. The effect is more pronounced for the oscillator than for the square-well.

In Fig. 9 and Fig. 10 we present the level scheme for the square well potential (2.11) with a finite potential step $(V_2 - V_0) = 60$ MeV and 40 MeV, resp. The finite internal potential step presents the possibility to study qualitatively the effect of a finite reduced density inside the bubble. In a classical description this was done in Ref. [5]. An

internal density distribution changes, of course, the surface tension of the LD at the inner surface and, to be consistent, we should also add a LD energy describing the macroscopic smooth energy originating from the internal density. The results of Fig. 9 and 10 are to demonstrate the effect of a reduced internal density on the level scheme. For this purpose we compare the level scheme in Fig. 9 and 10 with the one in Fig. 7:

(i) The density distribution extends from the inner surface down to $r = 0$ contrary to the case of the infinite square well of Fig. 7. Consequently, the weight of the inner contribution to the spin-orbit splitting increases as compared to the infinite square well. This is seen by the fact that the splitting in the unusual order tends to be larger in Fig. 9 and 10 as compared to Fig. 7.

(ii) For energies far below the step, the results are very similar to the ones of the infinite square well.

(iii) For energies above the step, the changes are of course very large the general tendency being a compression of the spectrum at energies above the step.

We would like to add a remark concerning the neutron (or proton) numbers which appear in the plots for the 3 values: 0.12, 0.24, 0.28 of the hole fraction parameter f, whenever the distance $\varepsilon_{\nu+1} - \varepsilon_\nu$ to the next higher s.p. energy exceeds 1.5 energy units. They represent the number of neutrons (or of protons) occupying s.p. states with energy $\varepsilon_k \leq \varepsilon_\nu$. Only if the total energy of the bubble nucleus has a minimum at one of these f-values, we may expect that the numbers given represent magic numbers for bubble nuclei. Nevertheless, they are useful to give us a hint as to where magic shell closures might occur. Clearly, the precise values of the magic numbers depend on the type of shell model used.

An interesting aspect can be observed concerning the dependence of the "magic numbers" on the hole fraction variable f. A general feature of all the level schemes as a function of f is the interplay of the steeply rising energies e_{nlj} with $n > 1$ and the smoothly f-dependent energies e_{1lj}. Magic numbers which appear in a region of many crossings depend sensitively on f, whereas magic numbers which occur between $1lj$-levels away from bunches of strongly rising $2lj$- and $3lj$-levels depend only weakly on f. The strongly f-dependent magicity occurs preferentially for small values of f, and the weakly f-dependent magicity for large f values.

3.3   The shell correction energy

From the spectrum of s.p. levels e_{nlj}^q we calculate the shell correction energy in the well-known way [13] $(\nu \equiv nlj; q = 1 : neutrons, q = 2 : protons)$

$$\delta E_{\text{shell}}(N, Z; f) = \sum_{q=1}^{2} \left(\int_{-\infty}^{\lambda_q} e g_q(e) de - \sum_{\nu} e_\nu^{(q)} \right) , \qquad (3.19)$$

where $g_q(e)$ is the average level density:

$$g_q(e) = \frac{1}{\gamma\sqrt{\pi}} \sum_\nu f_{corr}(u_\nu^{(q)}) \exp[-(u_\nu^{(q)})^2] \tag{3.20}$$

and f_{corr} is a 6th order correction polynomial of the variable $u_\nu^{(q)} = (e - e_\nu^{(q)})/\gamma$:

$$f_{corr} = 1 + (\frac{1}{2} - u_\nu^2) + (\frac{3}{8} - \frac{3}{2}u_\nu^2 + \frac{1}{2}u_\nu^4) + (\frac{5}{16} - \frac{15}{8}u_\nu^2 + \frac{5}{4}u_\nu^4 - \frac{1}{6}u_\nu^6) + ... \tag{3.21}$$

The position of the Fermi energy (λ_q) for the smooth energy spectrum is obtained by the integral:

$$N \text{ (or } Z) = \int_{-\infty}^{\lambda_q} g_q(e)\, de . \tag{3.22}$$

The "plateau condition" with respect the smearing width γ was reasonably well fulfilled.

In Fig. 11, we show the shell correction energy for the infinite square well as a function of the number of protons or neutrons. The hole fraction parameter is chosen to be f=0.24. The first substantial shell effect is seen to occur for N (or Z)=242. It corresponds to a negative shell energy of about $-15 \cdot \left[100/A^{2/3} \text{ MeV}\right]$. For a doubly magic nucleus the shell energy may amount to $(-25 \text{ to} - 30) \cdot \left[100/A^{2/3} \text{ MeV}\right]$. The magic numbers and the magnitude of the shell energy depend on the hole fraction f (see Figs. 17–19).

In Fig. 12, the dependence of the shell energy on the height of a constant potential in the internal region is studied: If only low-lying levels are occupied at a substantially lower energy than the step, the internal step has little influence. This is so for particle numbers ≤ 200. For larger numbers of N or Z, the magic numbers and the magnitude of the shell energy differ noticeably from the case of the infinite square well. In particular, the strong shell effect for 242 disappears completely whereas a new region of negative shell energy emerges at 330.

For comparison we show the shell energy for a shifted harmonic oscillator corresponding to the same hole fraction $f = 0.24$ in Fig. 13. The frequency of the oscillator was chosen for the particle number A=500 in Fig. 13. Strong shell effects are seen to occur for several numbers of particles of a given sort. They are not the same numbers as for the square well (of the same f), as one would expect. Nevertheless, corresponding shell closures are not very far away from each other and the order of magnitude of the shell energy is the same.

The dependence of the shell energy for given (N, Z) on the hole fraction f is shown in the 3-dimensional plots of Fig. 14 (for an infinite square well) and Figs. 15 and 16 (for a harmonic oscillator corresponding to A=500 and A=1000, resp.). It is seen that the magnitude of the shell energy increases with N (or Z). Each of the different islands of large negative shell energy corresponds to specific limited intervals of the hole fraction f. These intervals are of different length Δl depending on the specific magic number. On the average, the length $\Delta f \approx 0.05$. The fact that magic neutron or proton numbers for nuclear bubbles are correlated with given hole fraction values f and the fact that we expect the n- and p-distribution in a given bubble nucleus to exhibit the same shape,

limit the possible double magic combinations. Doubly magic numbers for neutrons and protons can only occur in a given bubble nucleus if they belong to the same value of the hole fraction f. This is analogous to the shell effects of ordinary nuclei as a function of the quadrupole deformation.

The correlation between particle number (N or Z) and f-parameter, which is visible in the Figs. 14–16, is shown once more in the form of undistorted 2-dimensional maps in Figs. 17–19.

For ordinary exotic nuclei, especially for nuclei with a large excess of neutrons over protons, the distribution of neutrons and protons do not always coincide. In fact the radius of the n-distribution is probably systematically somewhat larger than the one of the p-distribution ("n-skin"). For bubble nuclei with a large n-excess we have to expect the same phenomenon. Thus, for a very n-rich bubble nucleus, we expect that the inner (outer) radius of the n-distribution is smaller (larger) than the inner (outer) radius of the proton distribution. This relaxes somewhat the condition of equal f-parameter for n and p. We have neglected this possibility in our present investigation.

Let us now discuss the total energy:

$$E = E_{\mathrm{LD}} + \delta E_{\mathrm{shell}} , \qquad (3.23)$$

where E_{LD} is the liquid drop energy with a suitable choice of the reference energy. So far, we studied separately the dependence of E_{LD} and $\delta E_{\mathrm{shell}}$ on the hole fraction f for given N and Z. For this purpose we used the LD energy of a compact spherical nucleus (radius $R_0 = r_0 A^{1/3}$) as a reference energy (see Fig. 4)

$$\Delta E_{\mathrm{LD}} := E_{\mathrm{LD}}(f; N, Z) - E_{\mathrm{LD}}(f = 0; N, Z) \qquad (3.24)$$

because in this way the volume energy cancels due to the conventional saturation assumption.

If one adds $\delta E_{\mathrm{shell}}$ to ΔE_{LD} one finds bubble solutions in certain regions of the (N, Z)-plane. This is shown in Fig. 20.

The crucial question is the stability of these spherical bubble configurations with respect to deformations. A careful investigation of the stability versus volume conserving deformations of the inner (S_2) outer (S_1) surfaces of the bubble nucleus requires the calculation of the surface- and Coulomb energy of an arbitrarily shaped bubble and — what is much more difficult to achieve — the calculation of the eigenvalues of a correspondingly deformed single particle potential.

We have not yet performed such a calculation. It seems also a bit questionable to us whether such a big effort is meaningful in the framework of the Strutinsky method, given the fact that the Hartree-Fock theory (HF) and Hartree-Bogoliubov theory (HB) provide a quantitatively more reliable approach[2]. Instead, we applied a simple phenomenological method which had been introduced by W. Swiatecki [15] in 1966. The ansatz is designed

---

[2]The existence of stable bubble configurations for various mass– and charge numbers is being investigated within the HB-theory on the basis of the Gogny-interaction by J. F. Berger and J. Dechargé. Encouraging results were obtained by these authors (priv. com.).

so that the shell energy of the spherically symmetric nucleus is damped away as a function of the quadrupole deformation. The result is shown in Fig. 21 for a bubble nucleus of $A{=}750$ and $Z{=}288$ and a spherical bubble solution at $f{=}0.26$. The LD-energy at the spherical bubble shape is put equal to zero. The following features are of interest:

(i) The LD-energy decreases for positive as well as for negative values of the quadrupole deformation β_2 of the outer surface S_1.

(ii) Constraints on the shape of the surfaces (same deformations for the two surfaces or spherical inner surface S_2), results in noticeably higher energy than minimization of the LD-energy for given β_2 with respect to a limited number of shape degrees of S_1 and S_2. Even spurious flat minima on the oblate side are produced by these constraints.

(iii) $\delta E_{\text{shell}} + E_{\text{LD}}$ exhibit a deep and relatively narrow valley with a minimum of about –30 MeV at $\beta_2 = 0$. The shell effect disappears at about $\beta \approx \pm 0.2$ using Swiatecki's phenomenological form of δE_{shell}.

(iv) The barrier to fission is seen to be very thick. The spontaneous fission lifetime can safely be assumed to be practically infinite.

We can be sure that shell energies $\delta E_{\text{shell}} < $ -(20 to 30) MeV protect the spherical bubble nuclei from undergoing fission, i.e. lead to a practically infinite fission lifetime.

An important question is the dependence of our results on the parameters of the model: In the Strutinsky method, the surface tension σ and the radius parameter r_0 appear as phenomenological quantities. Apart from these two LD-parameters, which enter in a significant way (see Eq. (3.8')), the form of the phenomenological shell model and the parameters therein influence the results. We note that the dependence of the surface tension σ and the radius parameter r_0 on $((N-Z)/A)^2$ is of great importance for the stability regions of nuclear bubbles. Whereas we have some good empirical evidence on the isospin dependence of r_0 [16], very little is known about the isospin dependence of σ.

In order to test how the existence of bubble solutions depends on the parameters of the nuclear models we also performed a calculation based on Skyrme's energy density functional $E[\rho]$ for a spherical nucleus [17]. We have assumed that the kinetic energy density of protons τ_p and neutrons τ_n are functions of the corresponding nucleon densities

$$\tau_q(r) = \frac{\pi^{4/3} \cdot 3^{5/3}}{5} \rho_q^{5/3}(r) \quad \text{were} \quad q = p, n, \tag{3.28}$$

i.e. we have neglected the higher order correction which appears in the extended Thomas Fermi approximation. We represented the densities $\rho_n(r)$ and $\rho_p(r)$ of n and p by Fermi functions localized around $\bar{R} = \frac{1}{2}(R_1 + R_2)$

$$\rho_q(r) = \mathring{\rho}_q \left(\frac{1}{1 + exp\frac{r-R_1^q}{a_q}} - \frac{1}{1 + exp\frac{r-R_2^q}{a_q}} \right) \tag{3.29}$$

20

and determined the parameters R_1^q, R_2^q, and the surface thickness a_q by variation of $E[\rho]$.

Choosing the parameter set SkP proposed in Ref. [18] and considering a nucleus of A=470 and Z=184 we found the results shown in Fig. 22–25. To our surprise we obtained a beautiful bubble solution for a nucleus with twice the nucleon and proton number of $^{235}_{92}U_{143}$! This result is not obtained for the more conventional Skyrme parametrization SkIII. The specificity of the parameter set SkP is that the effective mass of the nucleon is equal to its free mass. This fit leads to a more realistic level density at low excitation energy than other Skyrme parametrizations. Here we are not pleading for or against the interaction SkP. We only learn from this calculation that the existence of bubble solutions for a given nucleus depends sensitively on the effective interactions we use. This is to be expected given the fact that the mass and charge of even the lightest bubble nuclei exceeds by far those of presently known nuclei.

The results displayed in Figs. 22–25 are clearly commented in the figure captions. We note in addition that the s.p. potential $V(r)$ obtained (see Fig. 23) is intermediate between a square well and a harmonic oscillator. Furthermore, we see that the energy density $h(r)$ shown in Fig. 25 drops more smoothly to zero at the inner and outer surface than it should for the leptodermous expansion to be valid. This demonstrates that the LDM should not be expected to yield a very precise value of the bubble energy, given the fact that the diameter d of the bubble layer is in general small.

Beside the absolute minimum of the energy as a function of the hole parameter f, one may find one or two competing equilibrium solutions at higher energy[3]. In Fig. 26 we show results on the system with Z=288 and N=462. The lowest solution is obtained for f=0.26, the 2nd one with an excitation energy of 5.9 MeV at f=0.175, and the 3rd one with an excitation energy of 25 MeV at f=0.12 . The difference between the total energy E and the LD–energy in Fig. 26 represents the shell energy. It is seen that the ground state solution is produced by a strongly negative shell energy in the region of f >0.24. Two other solutions are mainly produced by the appearance of a positive shell energy in the region of 0.13$\geq$ f $\geq$0.16 . By inspection of the level schemes (see esp. Fig. 7) one realizes that the strongly negative shell effect for f >0.24 is connected with a zone of reduced level density for Z=288 below the bunch of rising levels with 1 radial node. On the other hand, in the region 0.13$\geq$ f $\geq$0.16 the proton number 288 and the neutron number 462 correspond to Fermi energies which are located within the bunch of rising levels with 1 radial node.

4 Summary and discussion

We investigated the shell correction energy of spherical bubble nuclei. We found strong shell effects which may give rise to shell energies of up to -40 MeV for certain magic numbers. By calculating the LD-energy for deformed bubbles and assuming that the shell

---

[3]We owe this insight to J.F. Berger and J. Dechargé who found in their HFB calculations that up to 3 different bubble solutions may exist for the same number of neutrons and protons. For the solution with the smallest value of f, these authors find the hole to be occupied by a reduced nucleon density.

effect due to the spherical symmetry disappears as a function of the deformation in about the same way as for normal compact spherical nuclei, one finds that the fission barriers are of the same order of magnitude as the shell-correction energy for the spherical bubble solution. In favorable cases of magic numbers, this is sufficient to reduce the probability for spontaneous fission practically to zero.

The investigation shows that promising candidates for bubble nuclei are found for mass numbers $A \geq 450$, with the proton density being the larger the lighter the nucleus.

The origin of the shell effects is the high degeneracy of orbitals with large angular momentum on the one hand, and the rapid energetic increase of radial oscillation modes as a function of increasing bubble radius, on the other. The details of the results (for instance the lower limit of mass numbers, where bubble nuclei begin to exist or the precise value of magic numbers) depend sensitively on the choice of LD parameters and on the choice of the effective interaction, resp.

The spin-orbit splitting for bubble nuclei is smaller than for ordinary nuclei and the sign of the splitting may be reversed. The reason is that the inner and outer surface regions of the nuclear density distribution contribute to the splitting with opposite signs (see Fig. 24).

β-decays will tend to drive the system along isobaric lines to the composition with the largest total binding energy. For a number of systems this will lead to desintegration by fission after a series of β–decays. For systems where the shell effects vary strongly as a function of N and Z for given A, the β–decays will end up in a β–stable bubble composition.

Furthermore, a bubble nucleus consisting of N neutrons and Z protons may decay by emission of a neutron ($q=1$), a proton ($q=2$), or an α–particle ($q=3$), whenever these decay channels are open, i.e. whenever the corresponding Q_q–values are positive. Semi-classically, the decay probability per time unit $W_q(Q_q, l; N, Z)$ is given by the product of the penetrability $P_q(Q_q, l)$ of the potential barrier $U_q(r, l)$ and a quantity ω_q, which can be classically interpreted as the number of collisions per time unit of the particle q with the potential wall:

$$W_q = \omega_q P_q \, , \tag{4.1}$$

$$P_q(Q_q, l) = e^{-2J_q(Q_q, l)} \, , \tag{4.2}$$

$$J_q = \int_{r_1^{(q)}}^{r_2^{(q)}} dr \sqrt{\frac{2M_q}{\hbar^2} \left(U_q(r; l, Z_q) - Q_q \right)} \, . \tag{4.3}$$

Here, $M_{1(2)}=$ mass of the neutron (proton) $\approx M$, $M_3=$ mass of the α–particle, Q_q are the Q–values of the decay reactions, and U_q represent the potential barrier between the inner $(r_1^{(q)})$ and outer $(r_2^{(q)})$ turning points (see Fig. 27):

$$U_q = V_q(r) + \frac{\hbar^2 l(l+1)}{2M_q r^2} + \frac{Z_q(Z - Z_q)e_0^2}{r} \, . \tag{4.4}$$

Here, $V_q(r)$ is the average nuclear potential felt by the particle q, Z_q is its charge, Z is the charge of the mother nucleus, and l is the orbital angular momentum of the emitted

particle. The turning points $r_1^{(q)}, r_2^{(q)}$ are the solutions of the equation

$$U_q(r_{1,2}^{(q)}) = Q_q \; . \tag{4.5}$$

The frequency ω_q of assaults of the barrier may be estimated from the average velocity of particle q in the potential well prior to emission.

The potential $V_3(r)$ which acts on the composite α–particle is a rough phenomenological approximation of a non–local and energy–dependent potential. We calculated the penetrability for an α–particle through the barrier of ^{235}U, ^{252}Fm, and the barrier of the bubble nucleus consisting of 470 nucleons and 182 protons (2 times ^{235}U). For ^{235}U and ^{252}Fm we chose experimental Q–values ($Q_\alpha(^{235}U)$=4.647 MeV and $Q_\alpha(^{252}Fm)$=8.126 MeV) and Saxon–Woods type potential $V_q(r)$ with parameters adjusted by Huizenga and Igo [20]. For the bubble nucleus $^{470}182$ we used the Q-value 17.7 MeV which was obtained from our TF–calculation based on the Skyrme–functional and the special Skyrme interaction SkP (see Figs. 22 - 25). In all the cases the angular momentum l was chosen to be 0. The barriers and Q–values for 3 cases of α–decay are shown in Fig. 27. We obtained the following values of the α–decay half–life

$$T_\alpha = \frac{ln2}{W_3} \; . \tag{4.6}$$

Using the experimentally known values of $T_\alpha = 7 \cdot 10^8 y$ for ^{235}U and $T_\alpha = 25.4h$ for ^{252}Fm we have obtained $T_\alpha = 168s$ for $^{470}182$ by means of linear extrapolation in the $(J, log(T_\alpha))$ plane.

The system $^{470}182$ is a relatively light bubble nucleus. Note that we obtained this bubble solution only for the special Skyrme interaction SkP. As the mass and charge numbers of the bubble increases ($A > 750$, $Z > 250$), the Q_α–values tend to become larger, because the binding energy per nucleon in the bubble decreases. On the other hand, the height of the Coulomb barrier increases and the magicity of the mother nucleus may reduce the Q_α–value. The outcome is that the α–decay lifetime of heavy bubble nuclei may become much longer than the one we obtained for $^{470}182$.

The bubble nuclei we studied were usually stable with respect to emission of a neutron or a proton, as one can infer from the negative slope $\frac{dE^{LD}(N,Z)}{dN}$ and $\frac{dE^{LD}(N,Z)}{dZ}$. In the case of positive Q–values for p or n emission, the lifetimes can be estimated from the formulae (4.1)–(4.3). The decay probability W_q is smaller, the larger the angular momentum l of the emitted particle. Since rather large values of l occur in a typical bubble nucleus, the additional hindrance of the decay by the centrifugal barrier may become considerable.

Another important question is to investigate the stability of a given bubble nucleus as a function of temperature T and the angular momentum I of the system.

We can make the following qualitative remarks: As the temperature increases, the shell effect, which is essential for protecting the spherical bubble from fission decreases and is known to vanish more or less completely for $T \geq 1.5$ MeV. As far as LD part of the energy is concerned the main effect of a finite temperature is reduce the surface tension.

This increases the effective fissility parameter X_0 (see Eq. (3.8)) and thus tends to favour the spherical bubble solution as compared to the energy of the compact spherical drop (see Fig. 2). On the other hand, the reduced stiffness of the surface implies that the LD energy of the bubble decreases faster as a function of deformation (see Fig. 21). As a result, bubble nuclei cannot be expected to sustain a lot of excitation energy.

Concerning the dependence on the angular momentum again two effects have to be distinguished: The shell effect becomes a function of the rotational frequency ω_{rot} of the bubble. As a consequence, the maximal shell effect is expected to occur at a different value of the hole parameter f. Furthermore, the approximate effect of the rotation is to increase the total energy by the rotational energy of a rigidly rotating bubble. This rotational energy decreases as a function of f. Consequently, we may expect that an increase of the angular momentum of rotation lowers the energy of bubble valleys as compared to the energy of a rigidly rotating compact sphere. In specific cases, this effect may even produce a bubble valley where there would be none for angular momentum $I=0$ in very much the same way as this is the case for the 2nd valley in the region of rare earth nuclei. However, one should realize that the rotational energies for bubble nuclei are the smaller the larger the mass number A of the bubble nucleus. Consequently, for heavy long–lived bubbles we may not expect a large effect of the rotation. Another implication of the rotation will be that the optimal shape of the bubble will be deformed rather than spherical.

We have not yet taken into account pairing in bubble nuclei. For nuclei away from shell–closures we expect the pairing energy to be generally larger than for ordinary nuclei, because the density of levels in the vicinity of the Fermi energy is larger due to the high degeneracy of single particle states of large angular momentum. The pairing energy matters only if at least one sort of nucleons forms a closed shell, because otherwise bubble configurations are unstable. This means that the pairing in the bubble nucleus is expected to play a role only for the non–magic sort of nucleons. We do not expect that the pairing leads to a qualitatively important change of the stability.

It is of particular interest to investigate carefully the lower limits of mass- and charge number where sufficiently long-lived bubble nuclei can be expected. In view of the uncertainties concerning our knowledge of effective interactions, these predictions will always remain somewhat uncertain. Nevertheless, a lot of useful work can still be done. Assuming that one tries to produce a bubble nucleus of N_b neutrons and Z_b protons by a complete or incomplete fusion reaction

$$(N_1, Z_1) + (N_2, Z_2) = (N_b, Z_b)^\star + \cdots \tag{4.7}$$

the following aspects are important:

(i) As the compact spherical nucleus with about the same neutron and proton numbers N_b, Z_b is violently unstable with respect to fission and other decay channels, one may expect only a tiny fraction of the process to lead to an excited bubble nucleus.

(ii) Assuming that ΔT is the difference between the initial relative kinetic energy in the entrance channel and the energy $Z_1 Z_2 e_0^2 / (\mathring{R}_1 + \mathring{R}_2)$ of the Coulomb barrier

($\overset{\circ}{R}_i =$ radius of the incident nucleus (N_i, Z_i)), the total excitation energy E^* of the bubble nucleus can be estimated from the difference of the average binding energy per particle $B(N_i, Z_i)$ (< 0) of incident nuclei as compared to the average binding energy per particle $B(N_b, Z_b)$ of the bubble nucleus

$$E^* = [A_1 \cdot B(N_1, Z_1) + A_2 \cdot B(N_2, Z_2) - A_b \cdot B(N_b, Z_b)] - \Delta E + \Delta T \qquad (4.8)$$

Here ΔE is the energy carried away by the other final particles in the reaction (4.7). For typical bubble nuclei, the binding energy per particle is about -4 MeV as compared to -7 MeV for a heavy actinide nucleus. The bracket [ ] on the r.h.s. of (4.8) is then in general a negative number which is to be counterbalanced by the choice of the kinetic energy ΔT. Thus the energy of the beam particles must be chosen considerably higher than the Coulomb barrier in order to overcome the difference in binding energy of the constituants of the bubble as compared to ordinary nuclei.

We draw attention to the fact that for all examples of bubble nuclei we studied, the charge is "overcritical" [21]. This means that the binding energy of the lowest electronic state is larger than $2m_e c^2$. Consequently, whenever there is a K-shell vacancy in the nascent bubble, it will be spontaneously filled by an electron with simultaneous emission of a positon.

Acknowledgements

5   Appendix A1

Eigenfunctions of the shifted square well

The eigenfunctions φ_{nl} corresponding to the potential (2.11) have the form

$$\varphi_{nl}(r) = N_{nl} \cdot \begin{cases} f_l(\beta r) & \text{for } 0 \leq r < R_2 \\ a_{nl}\, j_l(\alpha r) + b_{nl}\, y_l(\alpha r) & \text{for } R_2 < r < R_1 \end{cases}, \qquad (A1.1)$$

where $f_l(\beta r)$ represents [10] the spherical Bessel function $j_l(\beta r)$ or the modified spherical Bessel function $\tilde{j}_l(\beta r)$ depending on the $sgn(\overset{\circ}{\varepsilon}_{nl} + V_1)$:

$$f_l(\beta r) = \begin{cases} j_l(\beta r) := \sqrt{\frac{\pi}{2\beta r}}\, J_{l+\frac{1}{2}}(\beta r) & \text{if } \overset{\circ}{\varepsilon}_{nl} + V_2 > 0 \\ \tilde{j}_l(\beta r) := \sqrt{\frac{\pi}{2\beta r}}\, I_{l+\frac{1}{2}}(\beta r) & \text{if } \overset{\circ}{\varepsilon}_{nl} + V_2 < 0 \end{cases}. \qquad (A1.2)$$

The functions $J_{l+\frac{1}{2}}(\beta r)$ and $I_{l+\frac{1}{2}}(\beta r)$ are the Bessel functions and the modified Bessel functions, respectively (see Ref. [10], Chap. 9 and 10). The parameter β is defined by

$$\beta = \left[\frac{2M|\overset{\circ}{\varepsilon}_{nl} + V_2|}{\hbar^2} \right]^{1/2}. \qquad (A1.3)$$

The dimensionless amplitudes a_{nl}, b_{nl} and the eigenenergies $\overset{\circ}{\varepsilon}_{nl}$ are determined by the boundary and continuity requirements

$$f_l(\beta R_2) = a_{nl}\, j_l(\alpha R_2) + b_{nl}\, y_l(\alpha R_2) \qquad (A1.4)$$

$$\beta f_l'(\beta R_2) = \alpha \left[a_{nl}\, j_l'(\alpha R_2) + b_{nl}\, y_l'(\alpha R_2) \right] \qquad (A1.5)$$

$$0 = a_{nl}\, j_l(\alpha R_1) + b_{nl}\, y_l(\alpha R_1). \qquad (A1.6)$$

Here and in what follows we use the notation:

$$j_l'(\alpha R_2) \equiv \left(\frac{\partial j_l(z)}{\partial z} \right)_{z=\alpha R_2} \qquad \text{and equally for} \quad y_l'(\alpha R_2), f_l'(\beta R_2).$$

We satisfy the eqns. (A1.6) by the ansatz

$$a_{nl} = \tilde{a}_{nl}\, y_l(\alpha R_1) \qquad (A1.7)$$

$$b_{nl} = -\tilde{a}_{nl}\, j_l(\alpha R_1) \qquad (A1.8)$$

The amplitude $\tilde{a}_{nl}$ is then obtained from (A1.4)

$$\tilde{a}_{nl} = \frac{f_l(\beta R_2)}{y_l(\alpha R_1)j_l(\alpha R_2) - j_l(\alpha R_1)y_l(\alpha R_2)}. \qquad (A1.9)$$

and the eigenenergies $\overset{\circ}{\varepsilon}_{nl}$ from the continuity of the logarithmic derivatives

$$\beta \frac{f_l'(\beta R_2)}{f_l(\beta R_2)} = \alpha \frac{y_l(\alpha R_1)j_l'(\alpha R_2) - j_l(\alpha R_1)y_l'(\alpha R_2)}{y_l(\alpha R_1)j_l(\alpha R_2) - j_l(\alpha R_1)y_l(\alpha R_2)}. \qquad (A1.10)$$

The overall normalization constant N_{nl} is of course defined by the condition (2.10).

6 Appendix A2

Eigenfunctions of the shifted harmonic oscillator

For $r < R_2$, the radial wave functions are again given by (A1.1) and (A1.2) up to a factor c_{nl} (see (A2.4)). At the point $r = R_2$, the radial wave function $\varphi_{nl}(r)$ in region I ($\varphi_{nl}^{\mathrm{I}}(r)$) and in region II ($\varphi_{nl}^{\mathrm{II}}(r)$) must be continuous and also its derivatives:

$$\varphi_{nl}^{\mathrm{I}}(R_2) = \varphi_{nl}^{\mathrm{II}}(R_2) \tag{A2.1}$$

$$\frac{d\varphi_{nl}^{\mathrm{I}}(R_2)}{dR_2} = \frac{d\varphi_{nl}^{\mathrm{II}}(R_2)}{dR_2} \,. \tag{A2.2}$$

Furthermore, $\varphi_{nl}^{\mathrm{I}}(r)$ must satisfy (2.5.2) at infinity.

The eigenvalues $\overset{\circ}{\varepsilon}_{nl}$ and the wave functions $\varphi_{nl}^{\mathrm{I}}(r)$ must be determined numerically or by the WKB approximation. In both cases it is convenient to introduce the radial functions $u_{nl}^{I}(\eta)$ depending on the dimensionless variable η

$$\eta = \gamma r = \sqrt{\frac{M\omega}{\hbar}} \cdot r \tag{A2.3}$$

for describing the functions $\varphi_{nl}(r)$ in region I:

$$\varphi_{nl}(r) = N_{nl} \begin{cases} c_{nl}\, f_l(\beta r) & \text{for } 0 \le r < R_2 \\ \frac{u_{nl}^{I}(\eta)}{\eta} & \text{for } r > R_2 \end{cases} \,. \tag{A2.4}$$

Henceforth, we shall suppress the subscripts nl for simplicity. The radial function $u^{\mathrm{I}}(\eta)$ satisfies the differential equation

$$\frac{d^2 u^{\mathrm{I}}(\eta)}{d\eta^2} - \left[\frac{l(l+1)}{\eta^2} + (\eta - \bar{\eta})^2 + \kappa \right] u^{\mathrm{I}}(\eta) = 0 \,, \tag{A2.5}$$

where

$$\bar{\eta} = \gamma \bar{R} \tag{A2.6}$$

$$\kappa := \frac{2(\overset{\circ}{\varepsilon} + V_0)}{\hbar\omega} \,. \tag{A2.7}$$

For large values of η, the centrifugal term $\frac{l(l+1)}{\eta^2}$ in (A2.5) is negligible and the equation (A2.5) assumes the standard form of the differential equation for parabolic cylinder functions (see Ref. [10], p. 686):

$$\frac{d^2 w}{d\xi^2} - \frac{1}{4}\xi^2 w(\xi) + \frac{\kappa}{2}\, w(\xi) = 0 \,, \tag{A2.8}$$

when introducing the new independent variable,

$$\xi := \sqrt{2}(\eta - \bar{\eta}) \,. \tag{A2.9}$$

27

The functions $u^{\mathrm{I}}(\eta)$ approach the solutions $w(\xi)$ of Eq. (A2.8)

$$u^{\mathrm{I}}(\eta) \to w(\kappa; \xi) = w[\kappa; \sqrt{2}(\eta - \bar{\eta})] \qquad (A2.10)$$

for η-values satisfying the inequality

$$\eta^2 (\eta - \bar{\eta})^2 \gg l(l+1). \qquad (A2.11)$$

For obtaining normalizable eigenfunctions $\varphi_{nl}(r)$ we need solutions $w(\xi)$ of the differential equation (A2.8) which go to zero at infinity ($\xi \to \infty$) at least $\sim \xi^{-1}$. The mathematical properties of the two basic, linearly independent solutions $y_{1,2}$ of Eq. (A2.8) (see Eq. (A2.13) and (A2.14) are described in Chapter 19 of Ref. [10]. The special linear combination which vanishes for $\xi \to \infty$ is given by

$$w(\kappa; \xi) = \sqrt{\pi} 2^{\frac{\kappa}{4}} \left[\frac{y_1(\xi)}{2^{\frac{1}{4}} \Gamma\left(\frac{3-\kappa}{4}\right)} - \frac{2^{\frac{1}{4}} y_2(\xi)}{\Gamma\left(\frac{1-\kappa}{4}\right)} \right] \qquad (A2.12)$$

$$y_1(\xi) = e^{-\frac{\xi^2}{4}} M\left(\frac{1-\kappa}{4}, \frac{1}{2}; \frac{\xi^2}{4} \right) \qquad (A2.13)$$

$$y_2(\xi) = \xi \, e^{-\frac{\xi^2}{4}} M\left(\frac{3-\kappa}{4}, \frac{3}{2}; \frac{\xi^2}{4} \right). \qquad (A2.14)$$

Here, $M(a, b; z)$ is the confluent hypergeometric function

$$M(a, b; z) = 1 + \frac{a}{b} \frac{z}{1!} + \frac{a(a+1)}{b(b+1)} \frac{z^2}{2!} + \cdots \qquad (A2.15)$$

It is interesting to consider the special case of $\kappa = 2n + 1$ (where $n = 0, 1, 2, \ldots$), where the functions $w(\kappa; \xi)$ become equal to the even Hermite functions for even n and to the odd Hermite functions for odd n (see Ref. [10], Eq. (19.13.1))

$$w(\kappa = 2n + 1; \xi) = e^{-\frac{1}{4}\xi^2} He_n(\xi) \qquad (A2.16)$$

$$He_n(\xi) := (-1)^n e^{\frac{\xi^2}{2}} \frac{d^n}{d\xi^n} \left\{ e^{-\frac{\xi^2}{2}} \right\}. \qquad (A2.17)$$

i.e. to the eigenfunctions of the linear harmonic oscillator. Of course, the functions $u^{\mathrm{I}}(\eta)$ do not even asymptotically tend to this limit because of the boundary conditions (A2.1-2) at $r = R_2$ and because of the centrifugal term in (A2.5). In the case of a general value of κ, the functions $w(\kappa; \xi)$ represent "parabolic cylinder functions" and are frequently denoted by (Ref. [10], Eq. (19.3.1)

$$w(\kappa; \xi) = \mathcal{D}_{\frac{1}{2}(\kappa-1)}(\xi). \qquad (A2.18)$$

For $|\xi| \gg \frac{|\kappa|}{2}$, they have the following asymptotic form (Ref. [10], (19.8.1)):

$$w(\kappa;\xi) \approx e^{-\frac{1}{4}\xi^2} \, \xi^{\frac{\kappa-1}{2}} \left\{ 1 - \frac{(\kappa-1)(\kappa-3)}{2^3\xi^2} + \frac{(\kappa-1)(\kappa-3)(\kappa-5)(\kappa-7)}{2^5 \cdot 4\xi^2} - \cdots \right\}.$$
(A2.19)

Solutions $u^{\mathrm{I}}(\eta)$ which tend asymptotically to the parabolic cylinder function $w(\kappa;\xi)$ (see (A2.10)) are thus normalizable for all values of κ.

The precise values of κ (or ε_{nl}) and of the amplitude a_{nl} are determined by the boundary conditions (A2.1-2). Substituting (A2.4) these boundary conditions read

$$c_{nl} \, f_l(\beta R_2) = \frac{u^{\mathrm{I}}_{nl}(\gamma_2 R_2)}{\gamma R_2}$$
(A2.20)

$$c_{nl} \, \beta \left(\frac{df_l(z)}{dz} \right)_{z=\beta R_2} = \gamma \cdot \left(\frac{\frac{du^{\mathrm{I}}_{nl}(\eta)}{d\eta} - u^{\mathrm{I}}_{nl}(\eta)}{\eta^2} \right)_{\eta=\gamma R_2}.$$
(A2.21)

The functions $u^{\mathrm{I}}_{nl}(\eta)$ can be determined numerically by the "shooting method".

7 Appendix A3

Thomas-Fermi approximation for eigenenergies ε_{nl} and single-particle densities $\rho_{nl}(r)$.

We mentioned already the WKB-approximation for the unperturbed eigenvalues ε_{nl} in Chapter 2. The Eq. (2.15) represents the simplest version of the WKB-approximation which contains no correction from the vicinity of the turning points nor from the classically forbidden regions. In what follows we only refer to this simplest version and claim that it can essentially also be obtained from the Thomas-Fermi approximation (TFA).

Let us first assume that a given eigenvalue ε_{nl} has been calculated from the simple semiclassical quantization condition (2.15) which we now write in the form

$$\sqrt{2M} \int_a^b dr \sqrt{\overset{\circ}{\varepsilon}_{nl} - U_l(r)} = \left(n + \frac{1}{2} \right) \hbar\pi,$$
(A3.1)

where the potential $U_l(r)$ is defined by

$$U_l(r) = \begin{cases} V(r) + \frac{l(l+1)\hbar^2}{2Mr^2} & \text{for neutrons} \\ V(r) + e_0 V_{Cb}(r) + \frac{l(l+1)\hbar^2}{2Mr^2} & \text{for protons} \end{cases}$$
(A3.2)

and where $n = 0, 1, 2, \ldots$.

As we stated already in Sect. (2.1), the Coulomb potential $V_{\mathrm{Cb}}(\vec{r})$ produced by the density distribution $\rho_p(\vec{r})$ of the protons (see Eq. (2.16)) can be easily evaluated in closed form if we approximate the density $\rho_p(\vec{r})$ by a uniform distribution in the bubble layer (see (2.18)). The result is given in Eq. (2.19).

The spin-orbit potential $\widehat{V}_{\text{SO}}$ ((2.33') or (2.37)) acting on eigenstates (2.2) in the coupled representation is a c-number operator. Consequently, in order to evaluate its mean value, we only need the single particle densities $\mathring{\rho}_{nl}(r)$ as defined in Eq. (2.40). Since no derivatives occur, the accuracy requirements concerning these single-particle densities are less stringent. Therefore, we determined these densities in the Thomas-Fermi approximation (TFA).

The numbers N of neutrons and Z of protons are related to the Fermi energies ε_F^n and ε_F^p by the Eqs. (2.25). On the other hand, the total densities $\mathring{\rho}_n(r)$, $\mathring{\rho}_p(r)$ of n,p must satisfy the trivial relations

$$N = \int d^3 r \; \mathring{\rho}_n(r) \,, \qquad (A3.3)$$

$$Z = \int d^3 r \; \mathring{\rho}_p(r) \,. \qquad (A3.4)$$

By comparison with (2.25) we obtain the TFA of the densities:

$$\mathring{\rho}_n(r) = \frac{2}{h^3} \int d^3 p \, \theta_0 \left[\varepsilon_F^n - \frac{p^2}{2M} - V(r) \right] = \frac{8\pi (2M)^{3/2}}{3h^3} [\varepsilon_F^n - V(r)]^{3/2} \qquad (A3.5)$$

$$\mathring{\rho}_p(r) = \frac{2}{h^3} \int d^3 p \, \theta_0 \left[\varepsilon_F^p - \frac{p^2}{2M} - V(r) - V_{\text{Cb}}(r) \right] = \frac{8\pi (2M)^{3/2}}{3h^3} [\varepsilon_F^p - V(r) - V_{\text{Cb}}(r)]^{3/2} \,. \qquad (A3.6)$$

By integrating over the phase space enclosed by two neighboring surfaces corresponding to the constant energies $\left(\varepsilon_\nu - \frac{\Delta\varepsilon}{2} \right)$ and $\left(\varepsilon_\nu + \frac{\Delta\varepsilon}{2} \right)$ we obtain the number of n or p contained in this phase space. Requiring that the volume is occupied by 1 n or p we may determine the corresponding energy width $\Delta\varepsilon$ which depends on the energy ε_ν and may be insignificantly different for n and p:

$$1 = \frac{1}{h^3} \int d^3 r \int d^3 p \, \theta_0 \left(\varepsilon_\nu + \frac{\Delta\varepsilon}{2} - \frac{p^2}{2M} - \tilde{V}(r) \right) \theta_0 \left(\frac{p^2}{2M} + \tilde{V}(r) - \varepsilon_\nu + \frac{\Delta\varepsilon}{2} \right) \,. \quad (A3.7)$$

Here $\tilde{V}(r)$ is the potential acting on a n or p, resp.:

$$\tilde{V}(r) = V(r) \qquad \text{for neutrons} \qquad (A3.8)$$

$$\tilde{V}(r) = V(r) + e_0 V_{\text{Cb}}(r) \quad \text{for protons} \,. \qquad (A3.9)$$

The density distribution $\mathring{\rho}(r; \varepsilon_\nu)$ of the neutrons (protons) in the energy layer is given by

$$\mathring{\rho}(r; \varepsilon_\nu) = \frac{2}{h^3} \int d^3 p \, \theta_0 \left(\varepsilon_\nu + \frac{\Delta\varepsilon}{2} - \frac{p^2}{2M} - \tilde{V}(r) \right) \theta_0 \left(\frac{p^2}{2M} + \tilde{V}(r) - \varepsilon_\nu + \frac{\Delta\varepsilon}{2} \right) \,. \quad (A3.10)$$

or

$$\mathring{\rho}(r; \varepsilon_\nu) = \frac{8\pi}{3h^3} (2M)^{3/2} \left[\left(\varepsilon_\nu + \frac{\Delta\varepsilon}{2} - \tilde{V}(r) \right)^{3/2} - \left(\varepsilon_\nu - \frac{\Delta\varepsilon}{2} - \tilde{V}(r) \right)^{3/2} \right] \,, \qquad (A3.11)$$

where the width $\Delta\varepsilon$ of the energy layer is to be determined from relation (A3.7). The condition (A3.7) reads more explicitly

$$1 = \frac{(4\pi)^2}{3h^3}(2M)^{3/2} \int dr\, r^2 \left[\left(\varepsilon_\nu + \frac{\Delta\varepsilon}{2} - \tilde{V}(r)\right)^{3/2} - \left(\varepsilon_\nu - \frac{\Delta\varepsilon}{2} - \tilde{V}(r)\right)^{3/2}\right]. \quad (A3.12)$$

In each case, integrations over the radial coordinate r extend over the interval where the integrand is real.

For calculating the average of the spin-orbit potential $\widehat{V}_{\text{SO}}$ we need the single particle density $\overset{\circ}{\rho}_{nl}(r)$ of a nucleon of given energy ε_{nl} and given orbital angular momentum l. The simple form (A3.11) of the density cannot be used because it averages over particles of all angular momenta l. From the TFA we cannot obtain a single particle density with the desired number n of radial nodes but we may obtain an approximate density distribution for a nucleon of given orbital angular momentum l by performing the integration in (A3.7) and (A3.10) under the constraint

$$\vec{L}^2 \equiv (\vec{r} \times \vec{p})^2 = l(l+1)\hbar^2. \quad (A3.12)$$

This can be simply achieved by choosing the 3-axis of the momentum integration in the direction of the position vector $\vec{r}$ and using cylinder coordinates in p-space:

$$\vec{p} = p_3\, \vec{e}_r + p_\perp(\cos\phi_p\, \vec{e}_1 + \sin\phi_p\, \vec{e}_2),$$

$$d^3p = dp_3\, dp_\perp p_\perp d\phi_p,$$

$$\vec{L}^2 = L^2 = r^2 p_\perp^2$$

$$\vec{p}^2 = p_3^2 + p_\perp^2 = p_3^2 + \frac{L^2}{r^2}.$$

The condition (A3.12) can be fulfilled conveniently by introducing the continuous dimensionless integration variable λ instead of $p_\perp$

$$p_\perp = \frac{L}{r} = \frac{\lambda\hbar}{r}$$

and inserting the δ-function $\delta\left(\lambda - \sqrt{l(l+1)}\right)$ into the integrals. We thus obtain the following 2 relations in analogy to the Eqs. (A3.7) and (A3.10)

$$
\begin{aligned}
1 =\ & \frac{\hbar^2}{h^3} \int d^3r \int dp_3\, d\lambda\, d\phi_p\, \frac{\lambda}{r^2}\, \theta_0\left(\varepsilon_{nl} + \frac{\Delta\varepsilon_l}{2} - \frac{p_3^2}{2M} - \frac{\lambda^2\hbar^2}{2Mr^2} - \tilde{V}(r)\right) \\
& \cdot\ \theta_0\left(\frac{p_3^2}{2M} + \frac{\lambda^2\hbar^2}{2Mr^2} + \tilde{V}(r) - \varepsilon_{nl} + \frac{\Delta\varepsilon_l}{2}\right) \delta\left(\lambda - \sqrt{l(l+1)}\right)
\end{aligned}
\quad (A3.13)
$$

$$
\begin{aligned}
\overset{\circ}{\rho}_{nl}(r;\varepsilon_{nl}) =\ & \frac{\hbar^2}{h^3 r^2} \int dp_3\, d\lambda\, d\phi_p\, \lambda\, \theta_0\left(\varepsilon_{nl} + \frac{\Delta\varepsilon_l}{2} - \frac{p_3^2}{2M} - \frac{\lambda^2\hbar^2}{2Mr^2} - \tilde{V}(r)\right) \\
& \cdot\ \theta_0\left(\frac{p_3^2}{2M} + \frac{\lambda^2\hbar^2}{2Mr^2} + \tilde{V}(r) - \varepsilon_{nl} + \frac{\Delta\varepsilon_l}{2}\right) \delta\left(\lambda - \sqrt{l(l+1)}\right).
\end{aligned}
\quad (A3.14)
$$

Carrying out the integrations in (A3.14) we obtain

$$\overset{\circ}{\rho}_{nl}\,(r;\varepsilon_{nl}) = \frac{2\sqrt{2M}\sqrt{l(l+1)}}{2\pi hr^2}\left\{\sqrt{\varepsilon_{nl} + \frac{\Delta\varepsilon_l}{2} - U_l(r)} - \sqrt{\varepsilon_{nl} - \frac{\Delta\varepsilon_l}{2} - U_l(r)}\right\}. \quad (A3.15)$$

where $U_l(r)$ represents the potential including the centrifugal term (see Eq. (A3.2)). For $l \gg 1$, we have $2\sqrt{l(l+1)} \approx 2l$. This represents the classical approximation for the quantum-mechanical degeneracy factor $((2l+1)$. The relation (A3.13) takes the form:

$$1 = \frac{2\sqrt{l(l+1)}2\sqrt{2M}}{h}\int dr\left\{\sqrt{\varepsilon_{nl} + \frac{\Delta\varepsilon_l}{2} - U_l(r)} - \sqrt{\varepsilon_{nl} - \frac{\Delta\varepsilon_l}{2} - U_l(r)}\right\}. \quad (A3.16)$$

The main deficiency of the TFA is to completely neglect the density in the classically forbidden region and to ignore the correct nodal structure of the density distribution of single particles inside the potential well.

The TFA is closely related to the WKB approximation. Let us consider the Hamiltonian

$$\widehat{H}_0 = -\frac{\hbar^2}{2M}\frac{d^2}{dx^2} + V(x) \quad (A3.17)$$

of a 1-dimensional potential model and the corresponding classical Hamiltonian function

$$\mathcal{H} = \frac{p^2}{2M} + V(x). \quad (A3.17')$$

If the particles moving in the potential $V(x)$ are fermions of spin $\frac{1}{2}$, the number $\mathcal{N}(\varepsilon_\nu)$ of fermions which fill the energy levels below a given energy ε_ν are given in the TFA by

$$\mathcal{N}(\varepsilon_\nu) = \frac{2}{h}\int dx\int dp\,\theta_0\,(\varepsilon_\nu - \mathcal{H}(x,p)). \quad (A3.18)$$

We can use the relation (A3.18) in order to determine approximate eigenvalues $\varepsilon_1 < \varepsilon_2 < \ldots$ by requiring $\mathcal{N}(\varepsilon_\nu)$ to be equal to 2ν, where $\nu = 1, 2, \ldots$ counts the eigenvalues in rising order. We thus obtain the implicit equation for determining the eigenvalues

$$\nu = \frac{1}{h}\int dx\int dp\,\theta_0\,(\varepsilon_\nu - \mathcal{H}(x,p)). \quad (A3.19)$$

For the linear harmonic oscillator $V(x) = \frac{M\omega^2}{2}x^2$ we find from (A3.19) the eigenvalues

$$\varepsilon_\nu = \nu\hbar\omega \quad (A3.20)$$

for $\nu = 1, 2, \ldots$. Using the same definition of the index ν, the correct eigenvalues are given by

$$\varepsilon_\nu = (\nu - \frac{1}{2})\hbar\omega. \quad (A3.21)$$

For the 1–dimensional infinite square well, the TFA (A3.19) yields the correct result. In the case of a spherical potential in 3-dimensional space we have to restrict the integration of the phase space to the hypersurface defined by the constraint (A3.12), i.e. we apply the method for calculation of the density distribution $\overset{\circ}{\rho}_{nl}$. This yields

$$n \cdot (2l+1) = \frac{\hbar^2 \cdot 2\pi \sqrt{l(l+1)}}{h^3} \int d^3r \int dp_3 \, \theta \left(\varepsilon_{nl} - \frac{p_3^2}{2M} - U_l(r) \right) \frac{1}{r^2} , \qquad (A3.22)$$

where $n = 1, 2, \ldots$ and $(2l+1)$ is the degeneracy of a level of given l. Within our approximation we should put $2\sqrt{l(l+1)} \approx 2l \approx 2l+1$. Consequently, (A3.22) takes the form

$$\sqrt{2M} \int_a^b dr \sqrt{\varepsilon_{nl} - U_l(r)} = n\hbar\pi , \qquad (A3.23)$$

where a and b are the lower and upper turning points and $n = 1, 2, \ldots$. The Eq. (A3.23) resembles the WKB formula given by Eq. (2.15). We note, however, that in (A3.23) the radial quantum number n starts from 1 whereas in (2.15) it starts from 0. For $n \gg 1$, the results are equivalent.

References

[1] H.A. Wilson, Phys. Rev. **69** (1946) 538.

[2] J. A. Wheeler, "Nucleonics Notebook", 1950 (unpublished), see also Ref. to Wheeler's toroidal nuclei in G. Gamow Biography of Physics (harper and Row, New York, 1961).

[3] P.J. Siemens and H.A. Bethe, Phys. Rev. Lett. **18** (1967) 704.

[4] C.Y. Wong, Ann. of Physics **77** (1973) 279.

[5] L.G. Moretto, K. Tso and G.J. Wozniak, Phys. Rev. Lett. **78**, 824 (1997).

[6] K. Dietrich and K. Pomorski, preprint nucl-th/9704061, submitted to Phys Rev. Lett.

[7] Private communication by J.F. Berger and J. Dechargé.

[8] Private communication by P. Bonche, P. H. Heenen and M. Weiss.

[9] M. Göppert-Mayer, H. J. D. Jensen, "Elementary Theory of Nuclear Shell Structure", New York – London, Wiley, 1955.

[10] Handbook of the Mathematical Functions, ed. by M. Abramowitz and I.A. Stegun, National Bureau of Standards, Applied Mathematics Series 55.

[11] A. Messiah, Quantum Mechanics, Vol. I, North Holland Publishing Company, 1961.

[12] P.Ring and P. Schuck, "The Nuclear Many Body Problem", New York 1980, Springer Verlag.

[13] P.G. Reinhard, H. Flocard, Nucl. Phys. **A584** (1995) 467.

[14] M. Brack, J. Damgaard, A.S. Jensen, H.C. Pauli, V.M. Strutinsky and C.Y. Wong, Rev. Mod. Phys. **44**, 320 (1972).

[15] W.D. Myers and W.J. Swiatecki, Nucl. Phys. **81** (1966) 1 and Ark. Fys. **36** (1966) 343.

[16] B. Nerlo–Pomorska and K. Pomorski, Z. Phys. **A348** (1994) 169; and M. Warda, B. Nerlo-Pomorska and K. Pomorski, to be published.

[17] D. Vautherin and D.M. Brink, Phys. Rev. **C5** (1972) 626.

[18] J. Dobaczewski, H. Flocard and J. Treiner, Nucl. Phys. **A422** (1983) 103.

[19] A.S. Dawydow, Theorie des Atomkernes, VEB Deutscher Verlag der Wissenschaftlen, Berlin 1963.

[20] J.R. Huizenga and G. Igo, Nucl. Phys. **29** (1962) 462.

[21] B. Müller, Ann. Rev. Nucl. Scien. **26** (1976) 26.

Figures captions.

1. The function $v_2(X_0)$ defining the stationary points of the energy $\mathcal{E}(v_2; X_0)$ as a function of the fissility parameter X_0.

2. Difference $\mathcal{E} = \Delta E_{\mathrm{LD}}/E_S(R_0)$ of the LD energy of a bubble of reduced inner radius v_2 and the LD energy of a compact spherical nucleus of radius R_0.

3. Lines of equal bubble fissility parameter X in the (N, Z) plane. Isobars are indicated by the parallel straight lines.

4. Lines of equal binding energy gain ΔE_{LD} by bubble formation. Parallel straight lines indicate isobars.

5. Lines of equal hole fraction f in the (N, Z) plane. Parallel straight lines indicate isobars.

6. Lines of constant LD–binding energy per particle. Parallel straight lines indicate isobars.

7. Level scheme for the shifted infinite square well with the spin–orbit coupling as a function of the hole fraction $f = (R_2/R_1)^3$ (see Eq. (3.15)). The letters s, p, d, f, g, h, i, j, ... mean the orbital angular momenta $l = 0, 1, ...$. For 3 values of f (0.12, 0.24, 0.28) numbers are written just above certain single particle energies ε_ν whenever the distance $(\varepsilon_{\nu+1} - \varepsilon_\nu)$ exceeds 1.5 energy units. They represent the number of neutrons (or of protons) occupying single particle states with energy $\varepsilon_k \leq \varepsilon_\nu$.

8. Level scheme for the shifted harmonic oscillator with spin–orbit coupling as a function of the hole fraction f. The oscillator frequency ω was determined as a function of f for A=500.

9. Level scheme for the infinite square well potential with a finite step in the inner region. Height $(V_0 - V_2)$ of the step: 60 MeV for $r < R_2$.

10. Same as in Fig. 9, but with a step height of 40 MeV.

11. Shell correction energy δE_{shell} for bubbles with f=0.24 as a function of N or Z for the shifted infinite square well with spin–orbit term.

12. Same as in Fig. 11, but for a square well with an internal step height $(V_0 - V_2)$= 40, 50, and 60 MeV. The case of the simple infinite square well is given again for comparison.

13. Same as in Fig. 11, but for a shifted harmonic oscillator potential. The oscillator frequency corresponds to the mass number A=500.

14. Shell energy evaluated from the infinite square well plus $\vec{l}\cdot\vec{s}$–term as a function of N (or Z) and the hole fraction f. The energy units are $[100/A^{2/3}]$ MeV.

15. As in Fig. 14, but for a shifted harmonic oscillator potential corresponding to the particle number $A{=}500$. Energy unit: MeV.

16. As in Fig. 14, but for a shifted harmonic oscillator potential corresponding to the particle number $A{=}1000$. Energy unit: MeV.

17. Lines of constant shell energy as a function of particle number (N or Z) and the hole fraction parameter f for a shifted infinite square plus $\vec{l}\cdot\vec{s}$–coupling. The energy unit is $[100/A^{2/3}]$ MeV.

18. As in Fig. 17, but for a shifted harmonic oscillator with $\vec{l}\cdot\vec{s}$–coupling. The oscillator frequency corresponds to the particle number $A{=}500$. Energy unit: MeV.

19. As in Fig. 18, but with the oscillator frequency chosen for the mass number $A{=}1000$.

20. The map of the liquid drop plus the shell correction energy corresponding to the bubble solution.

21. LD–energy (solid line), shell correction energy (dotted line), and the total energy (dashed dotted line) as a function of the quadrupole deformation β_2 of the outer bubble surface S_1. The LD–energy is minimized with respect to the multipole deformation of the order 4 and 6 of the surface S_1 and the multipole deformation 2 to 6 of the inner surface S_2. The long dashed line represents the LD-energy when both surfaces have the same deformation. The short dashed line corresponds to the case when the inner surface is a sphere.

22. Density $\rho_p(r)$ of protons (solid line) and $\rho_n(r)$ of neutrons (dashed line) obtained by variation of the Skyrme functional (3.28) obtained within the EFT approximation for SkP forces and for the nucleus Z=184, A=470.

23. Nuclear central s.p. potential acting on protons (solid line) and neutrons (dashed line) as obtained from the variation of the Skyrme energy functional [17].

24. Average spin–orbit potential $V_{LS}(r)$ for $A{=}470$ and $Z{=}184$.

25. Energy density $h(r)$ for $A{=}470$ and $Z{=}184$.

26. Total energy E and liquid drop energy E_{LD} as a function of the hole parameter f for a system with $Z{=}288$ protons and $A{=}750$ nucleons. 3 bubble solutions corresponding to the f-values $f{=}0.26$ (ground state), $f{=}0.175$ (bubble valley at the excitation energy $E^*{=}5.9$ MeV), and $f{=}0.12$ (bubble valley at the excitation energy $E^*{=}25$ MeV) are seen to exist. The inner and outer radii of the 3 solutions are: $R_2{=}7.69$ fm and $R_1{=}12.05$ fm for $f{=}0.26$, $R_2{=}6.50$ fm and $R_1{=}11.62$ fm for $f{=}0.175$, $R_2{=}5.61$ fm and $R_1{=}11.37$ fm for $f{=}0.12$.

27. The potential barrier $U_3(r)$ acting on an α–particle in ^{235}U, in ^{252}Fm, and in the bubble nucleus $^{470}184$ are shown together with the corresponding $Q_3 = Q_\alpha$ values. The bubble nucleus $^{470}184$ is the one obtained as a result of a TF–calculation with the Skyrme interaction SkP (see Figs. 22 - 25).
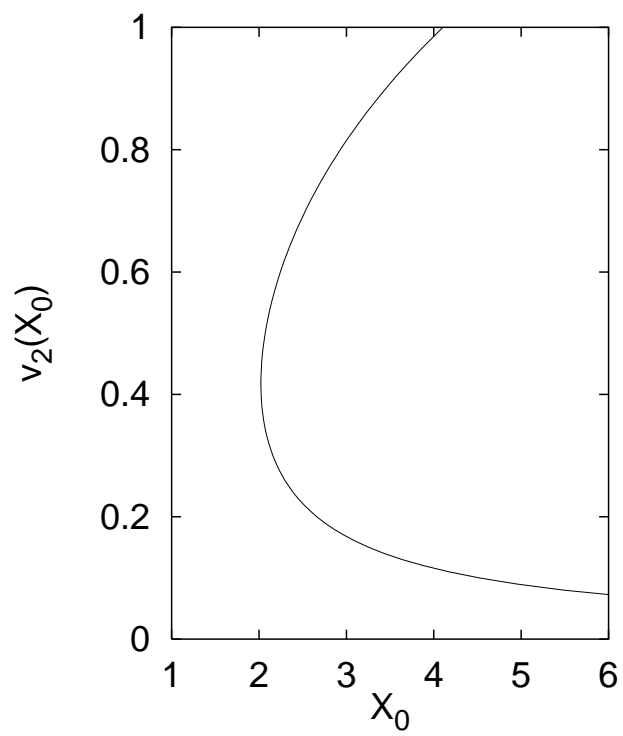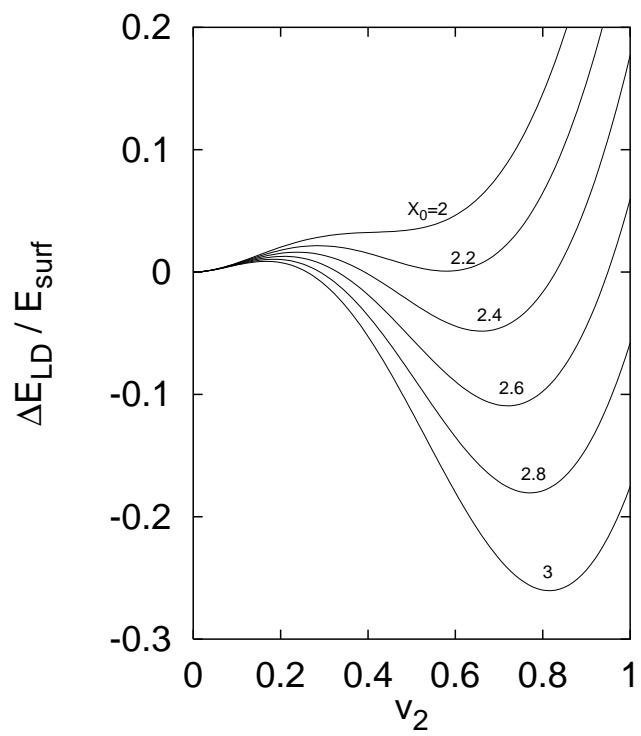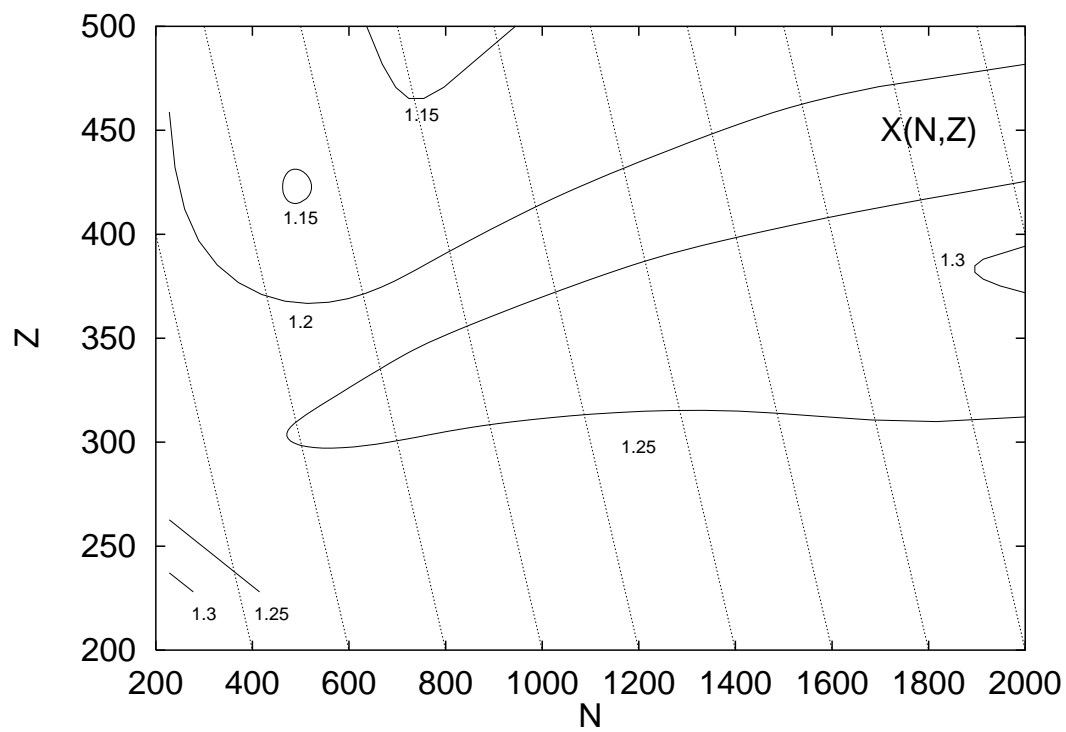
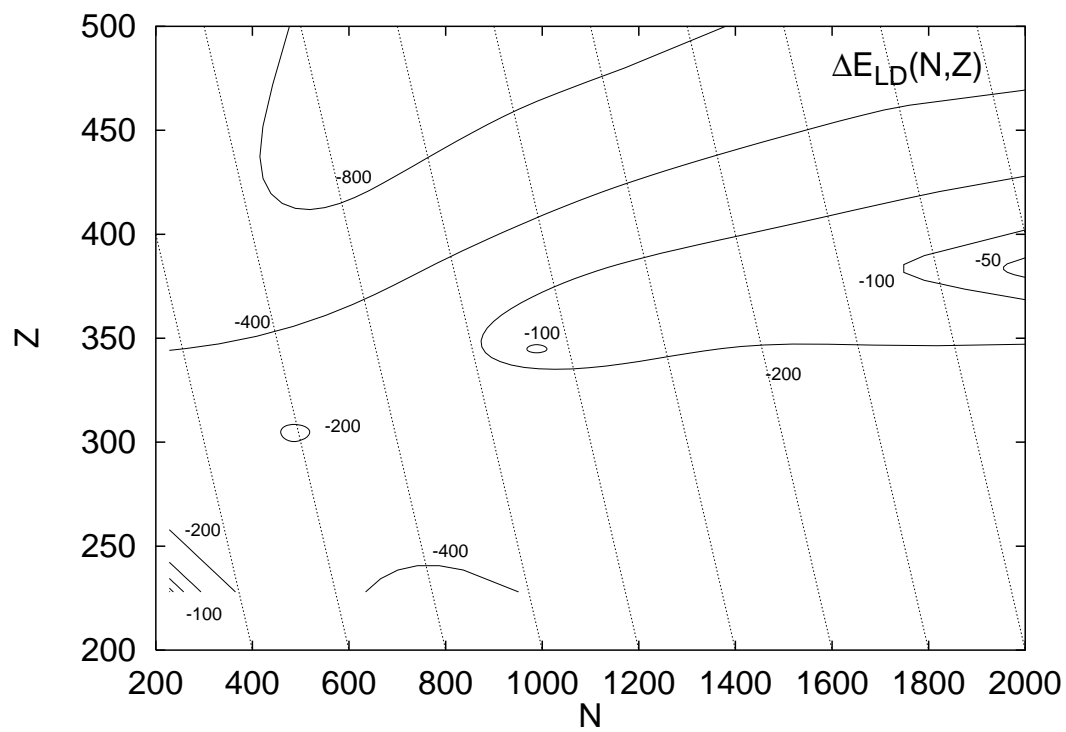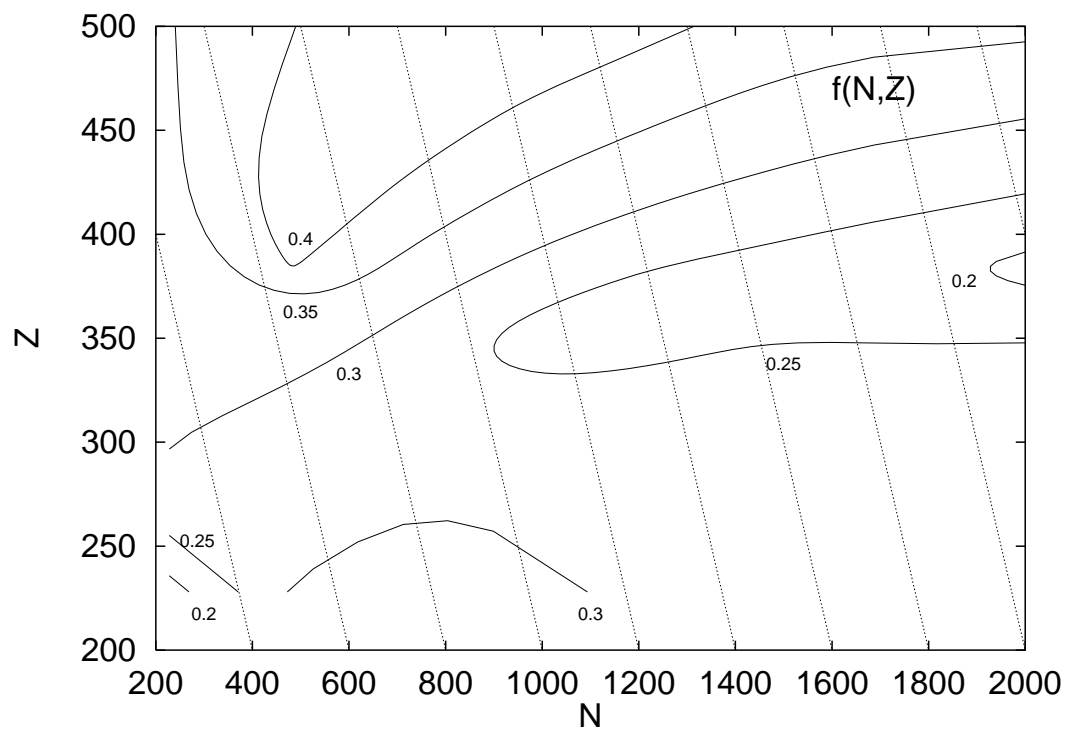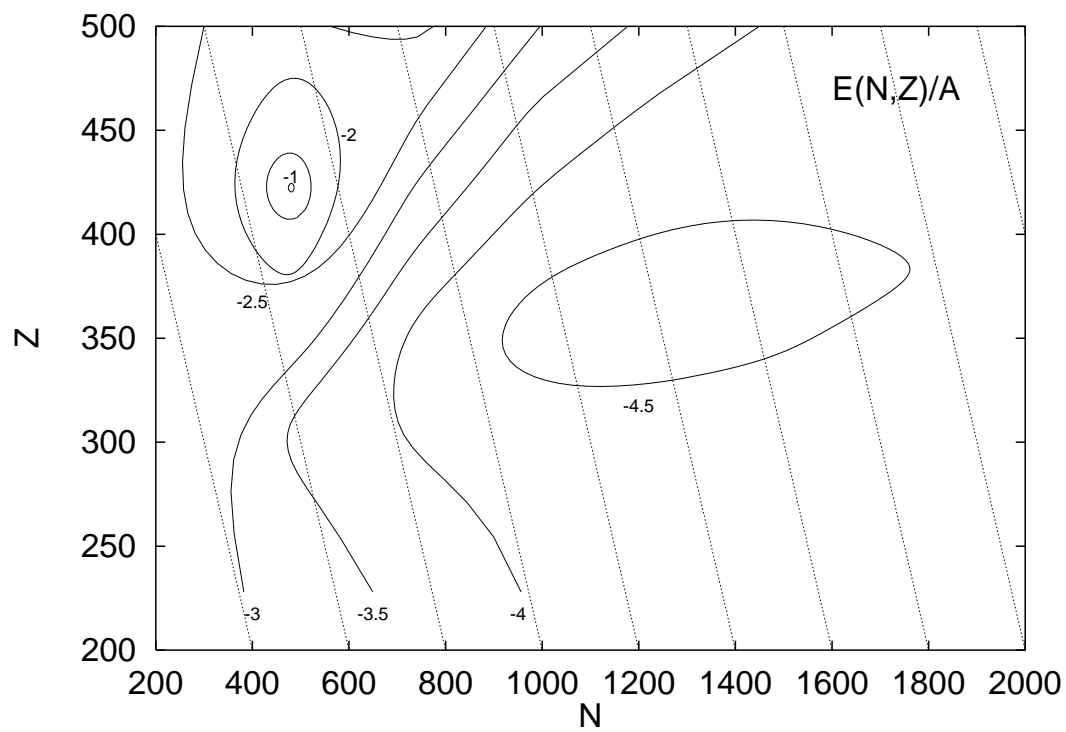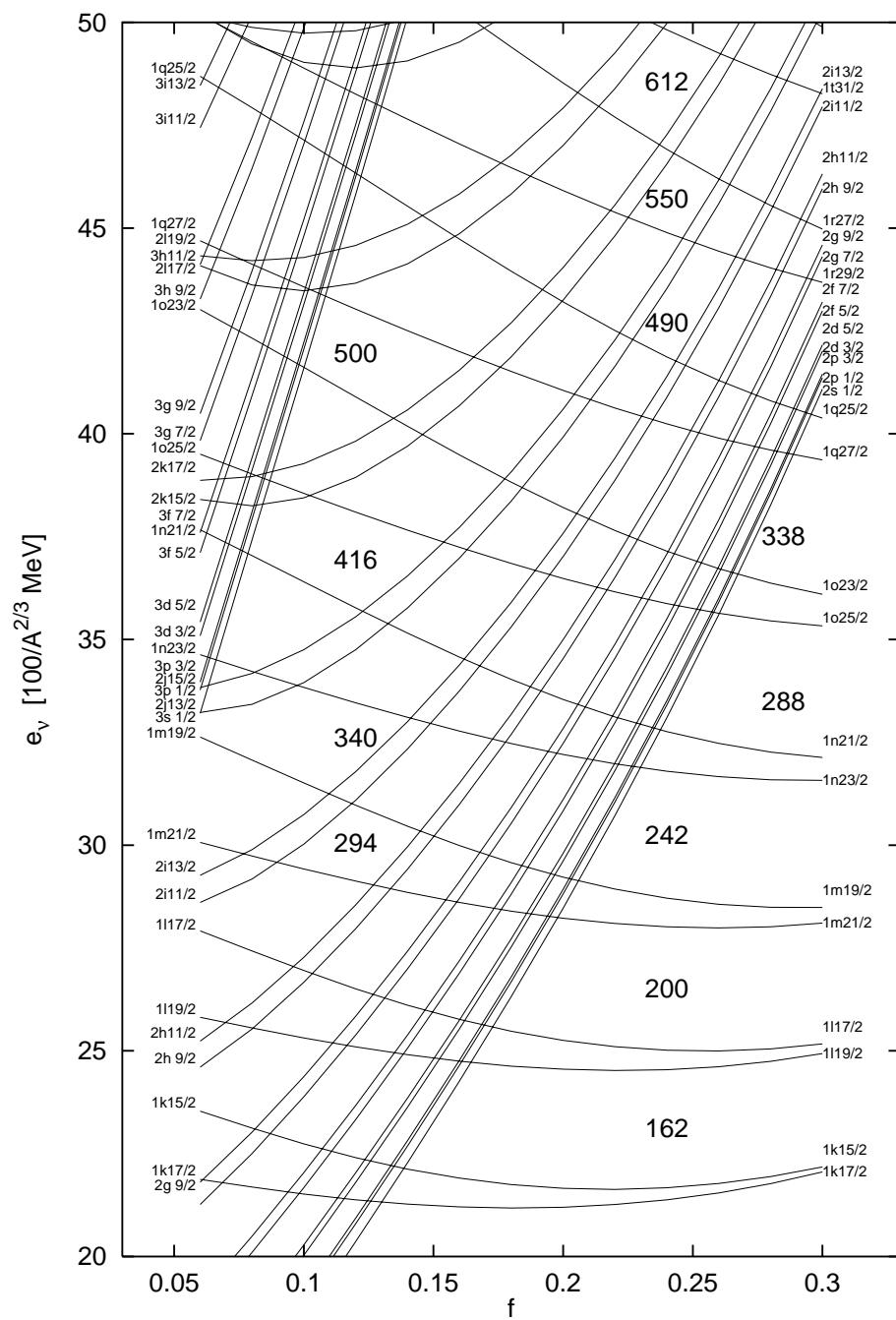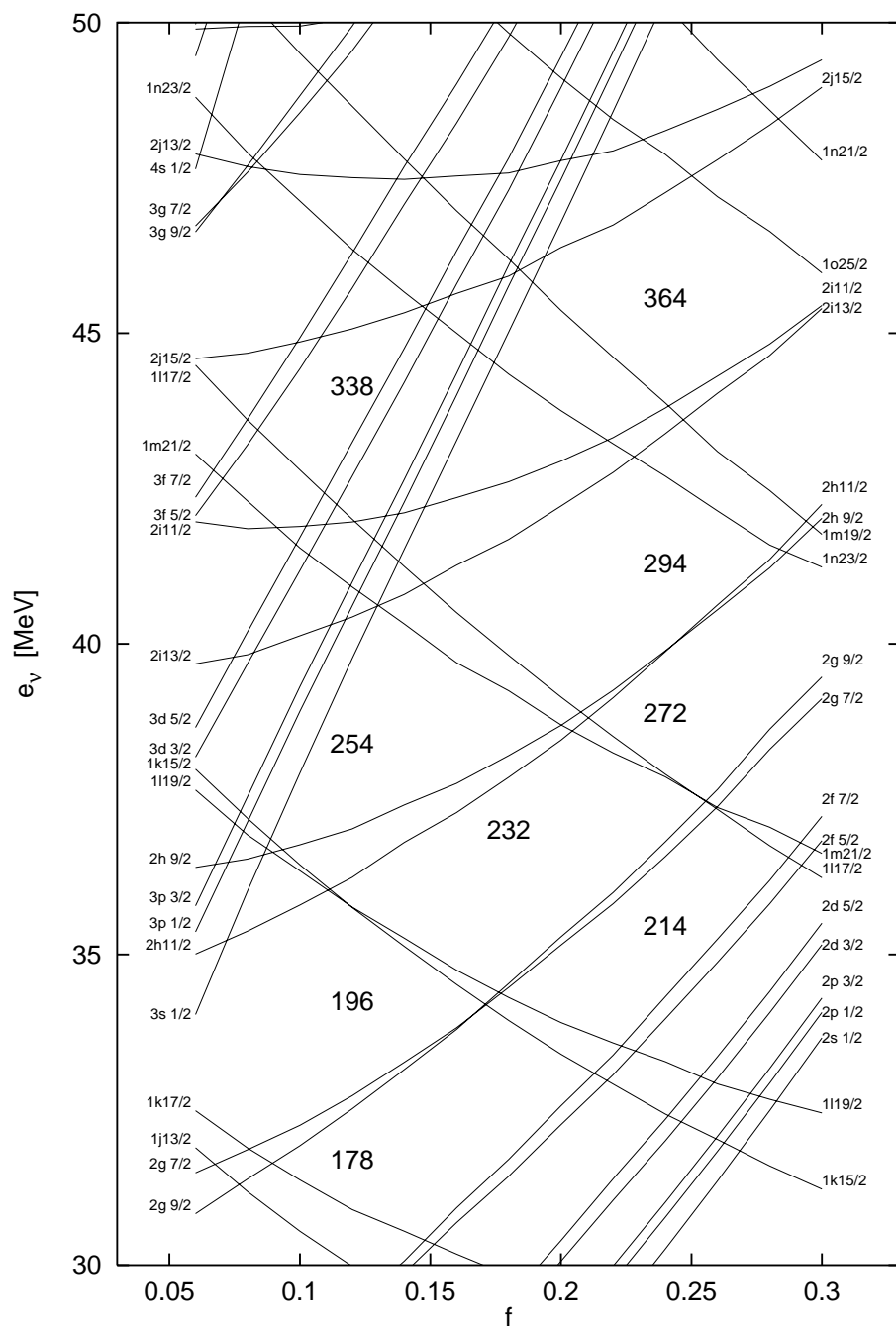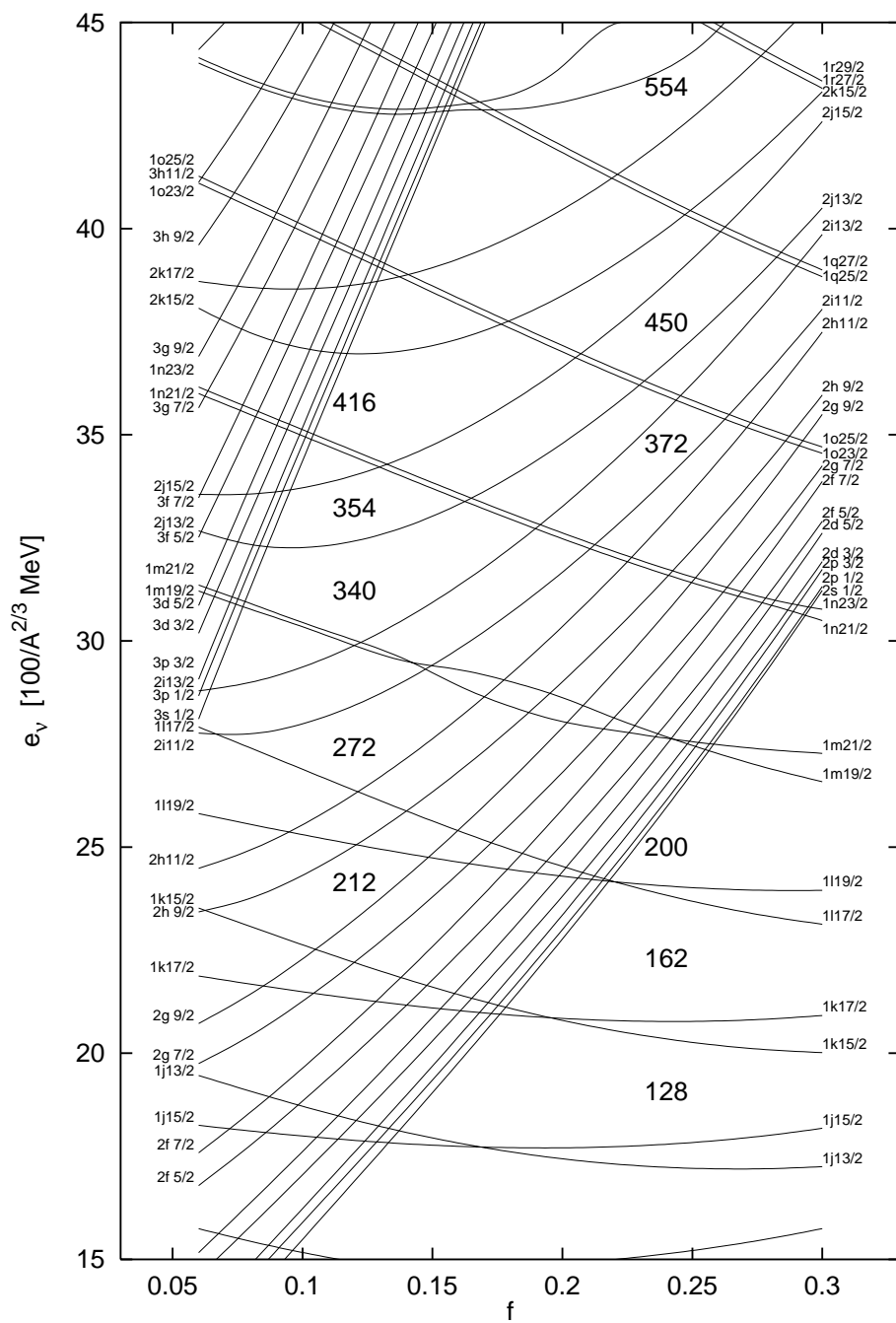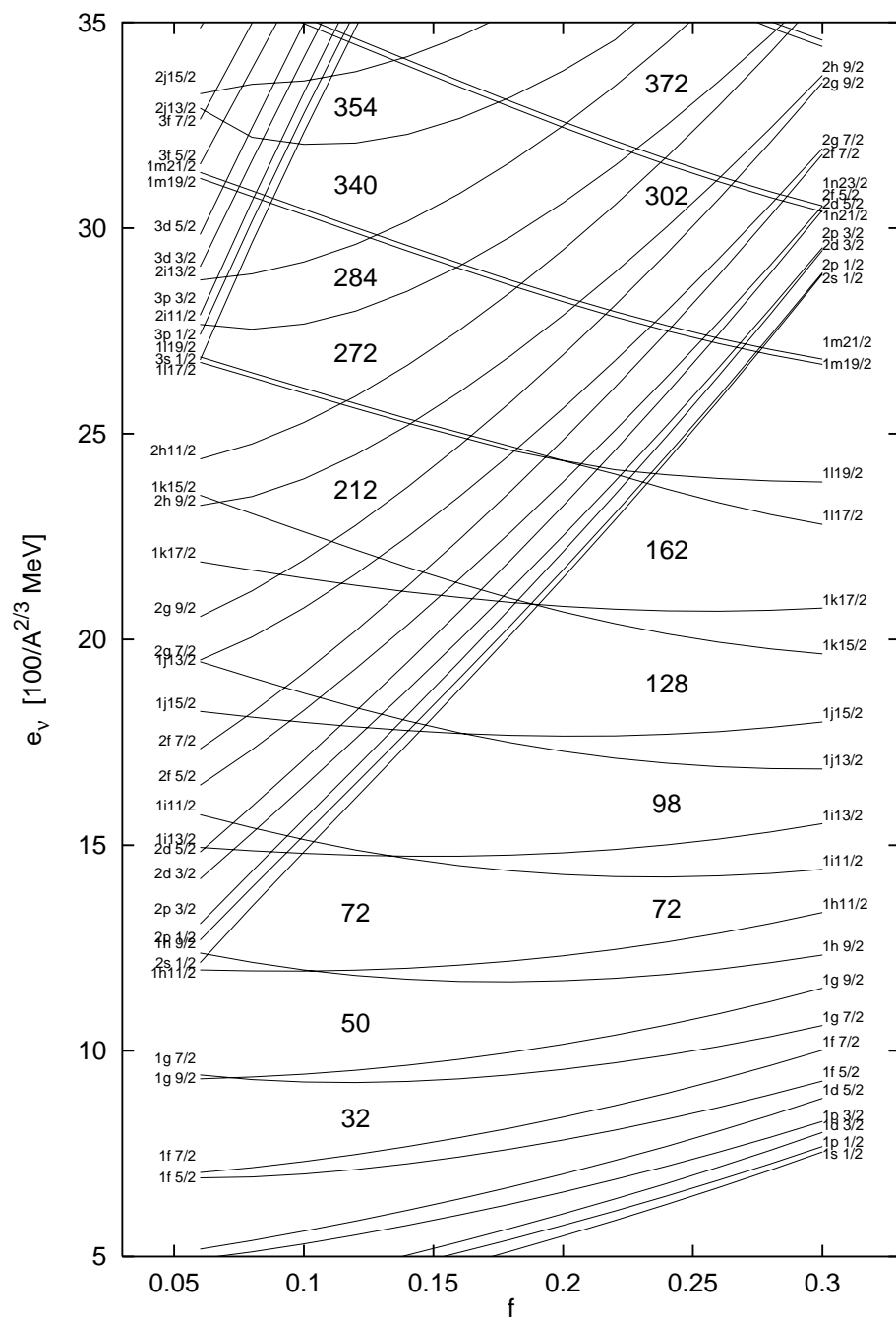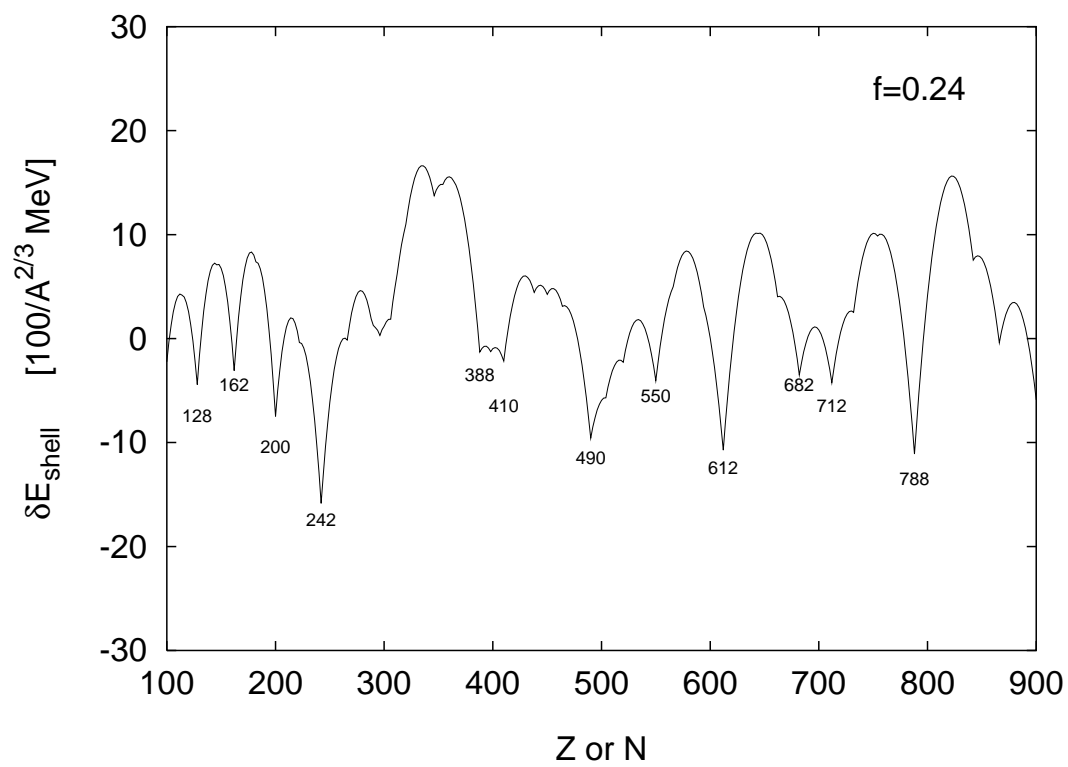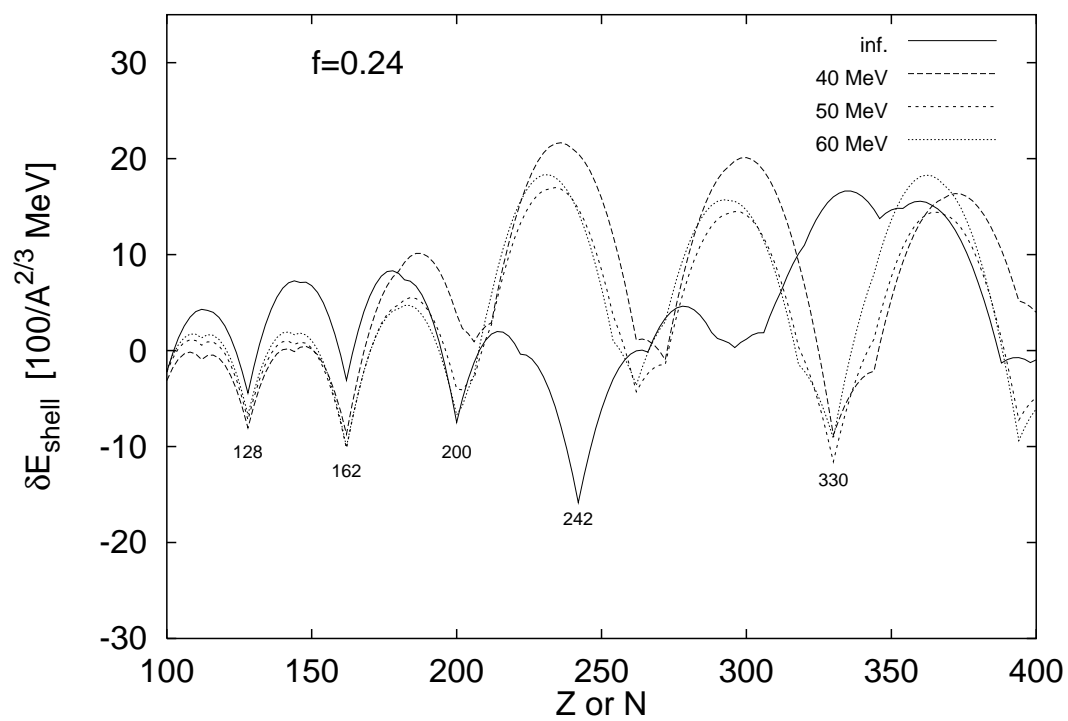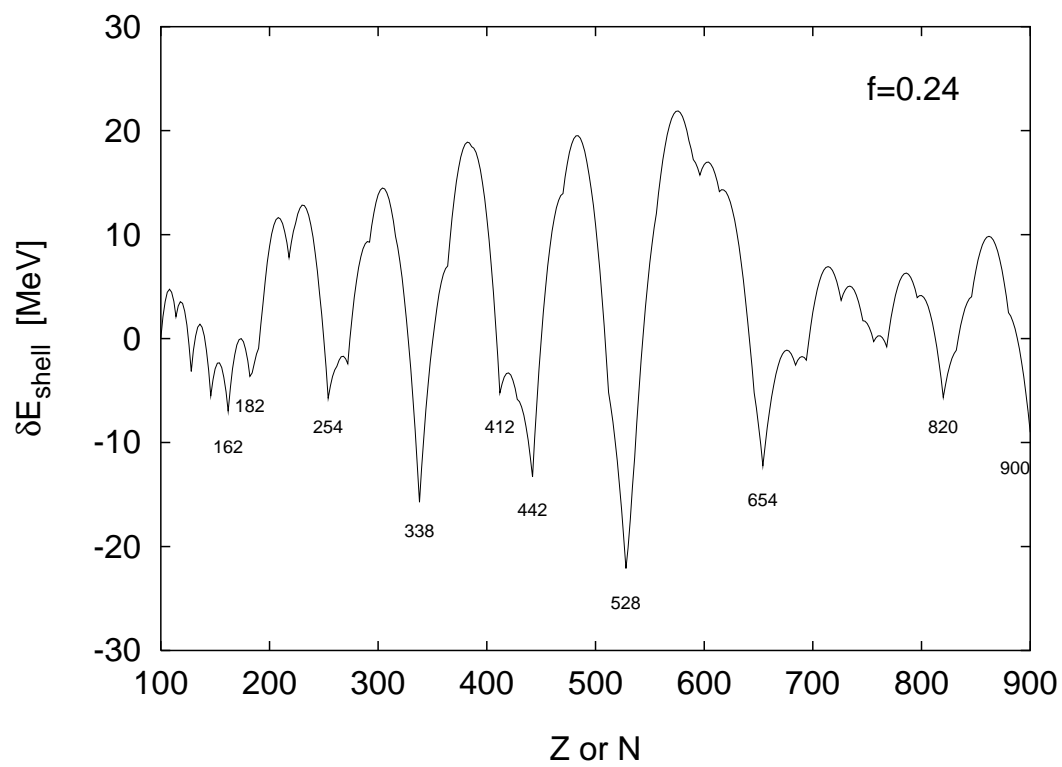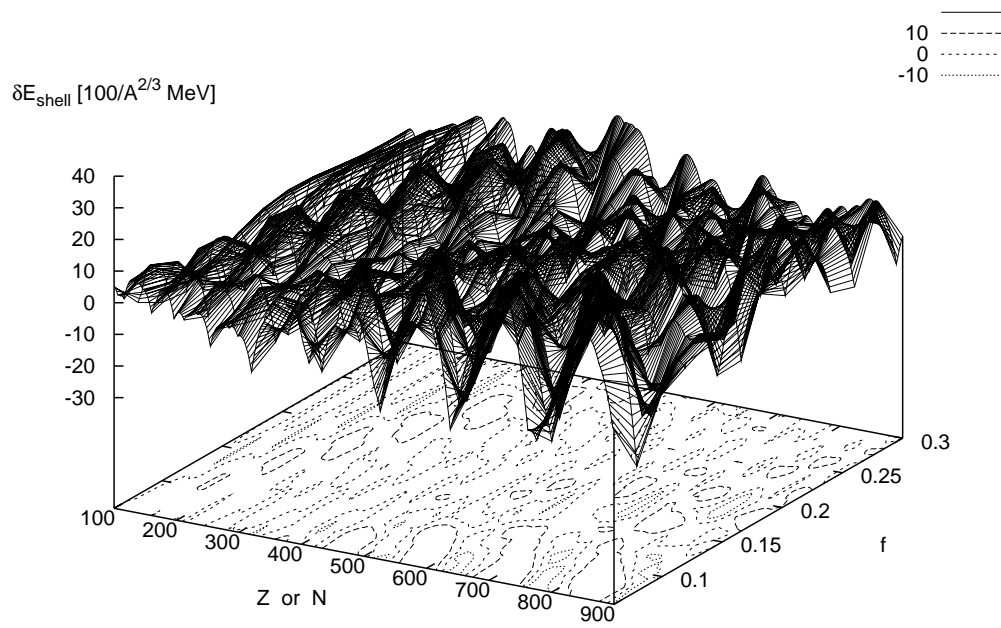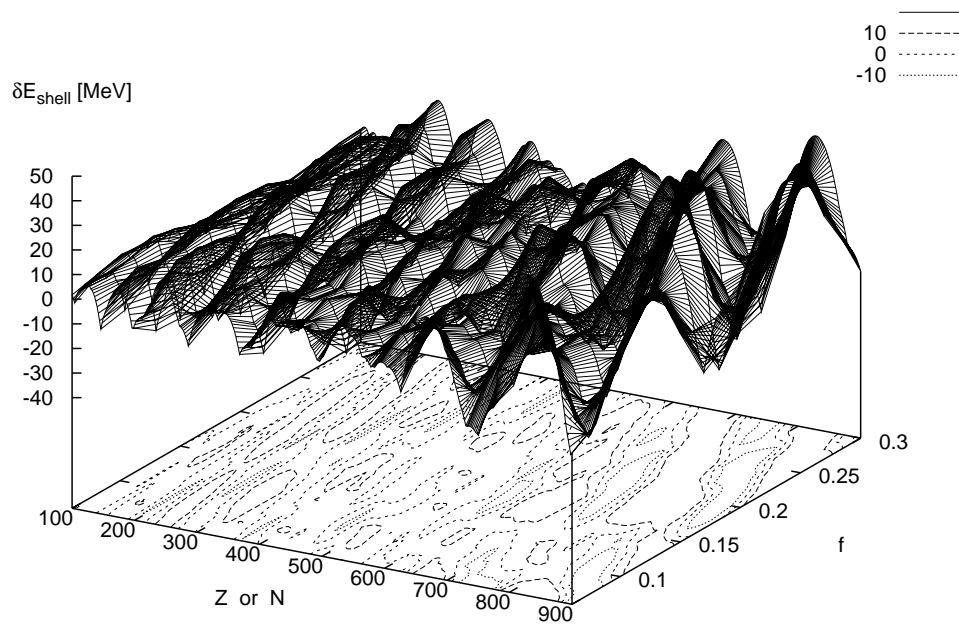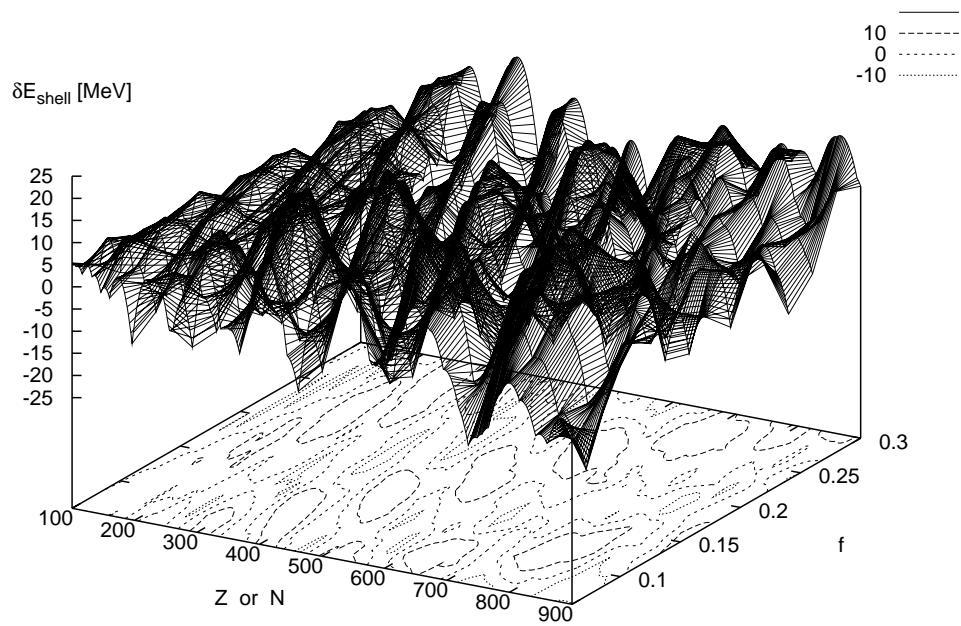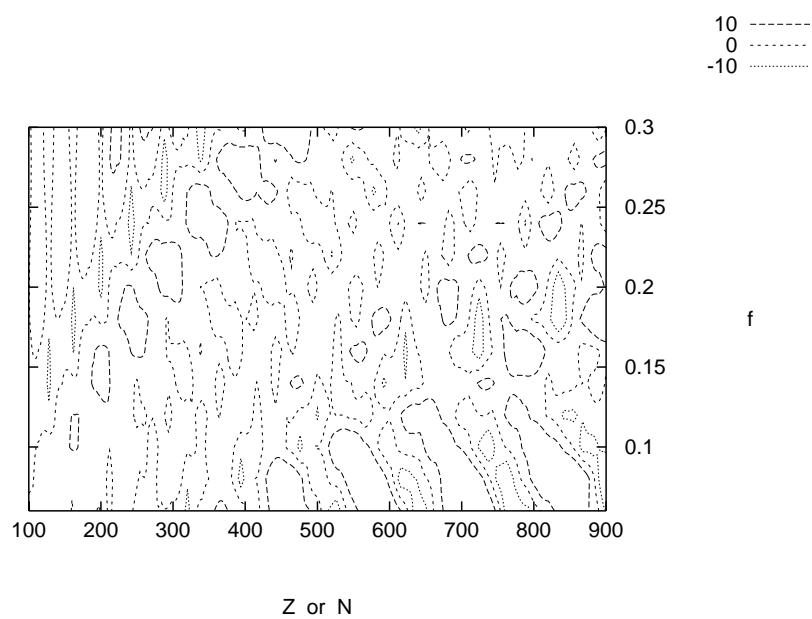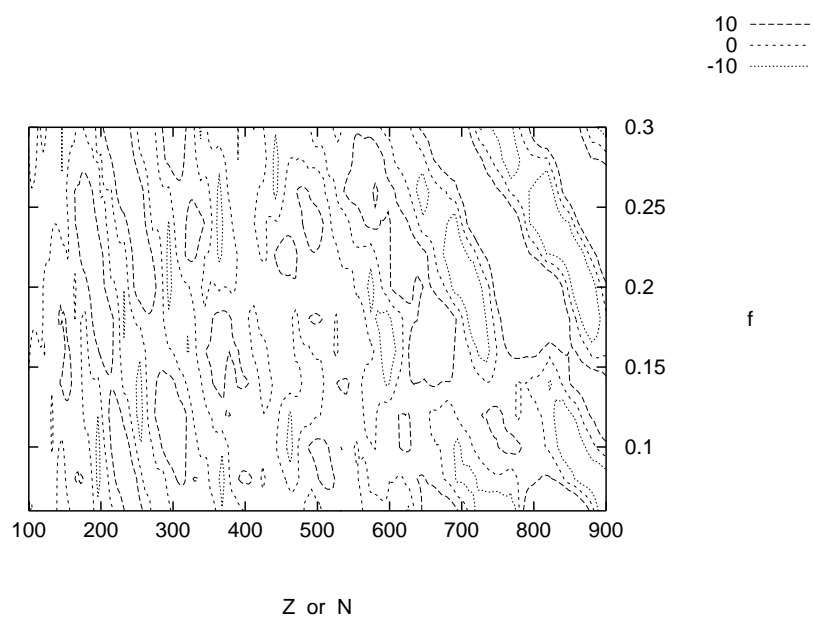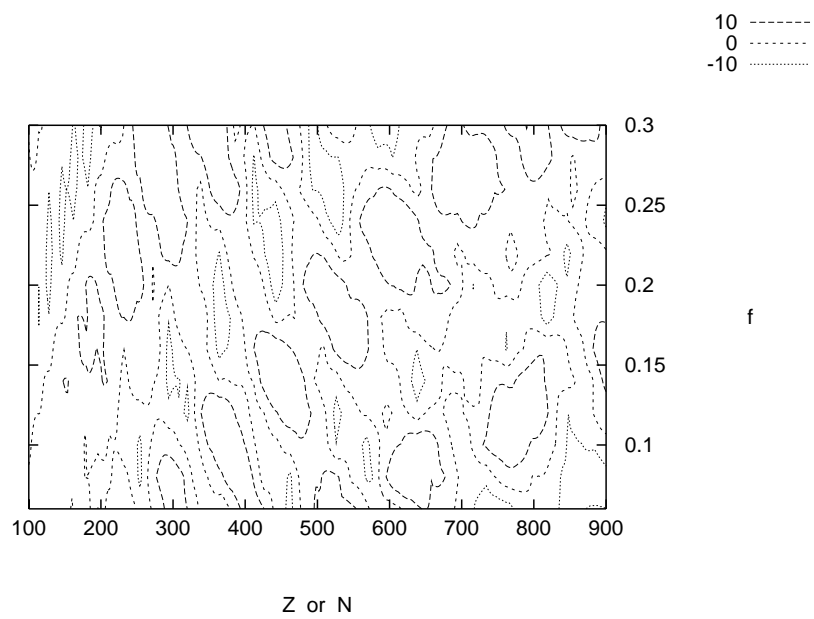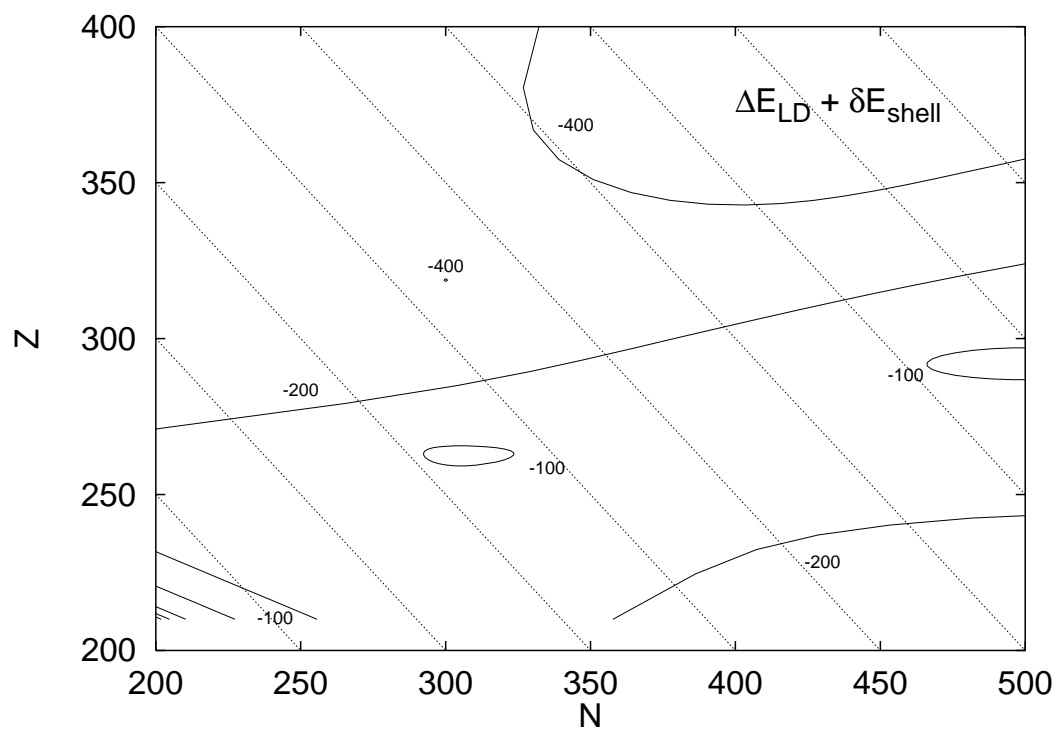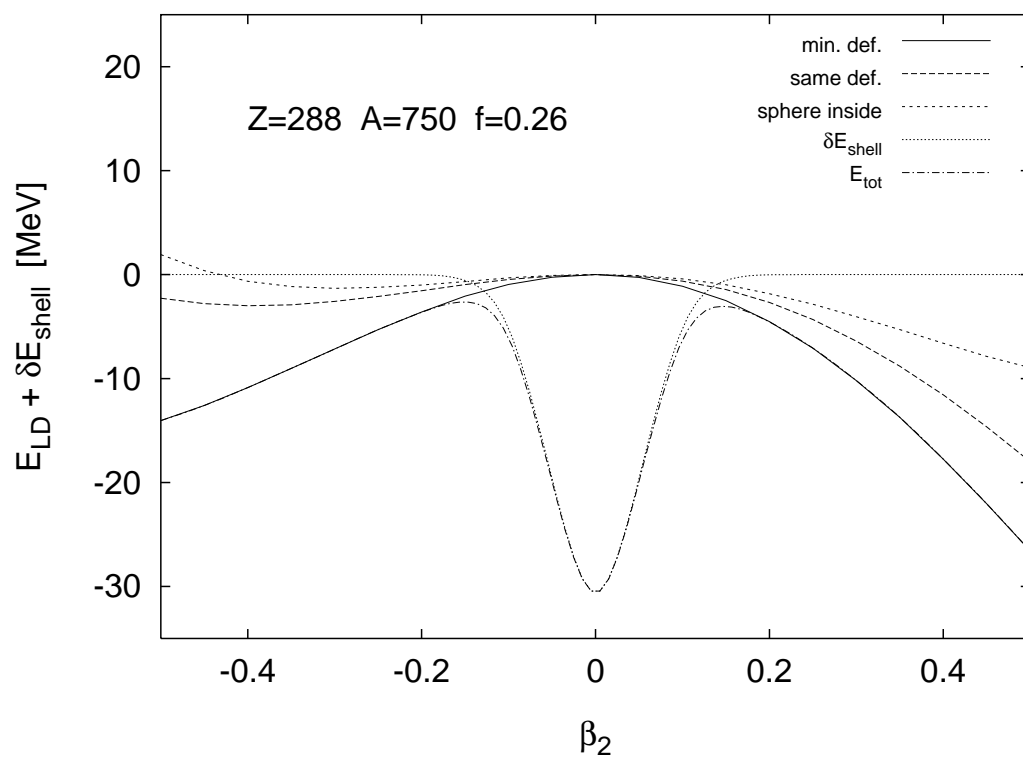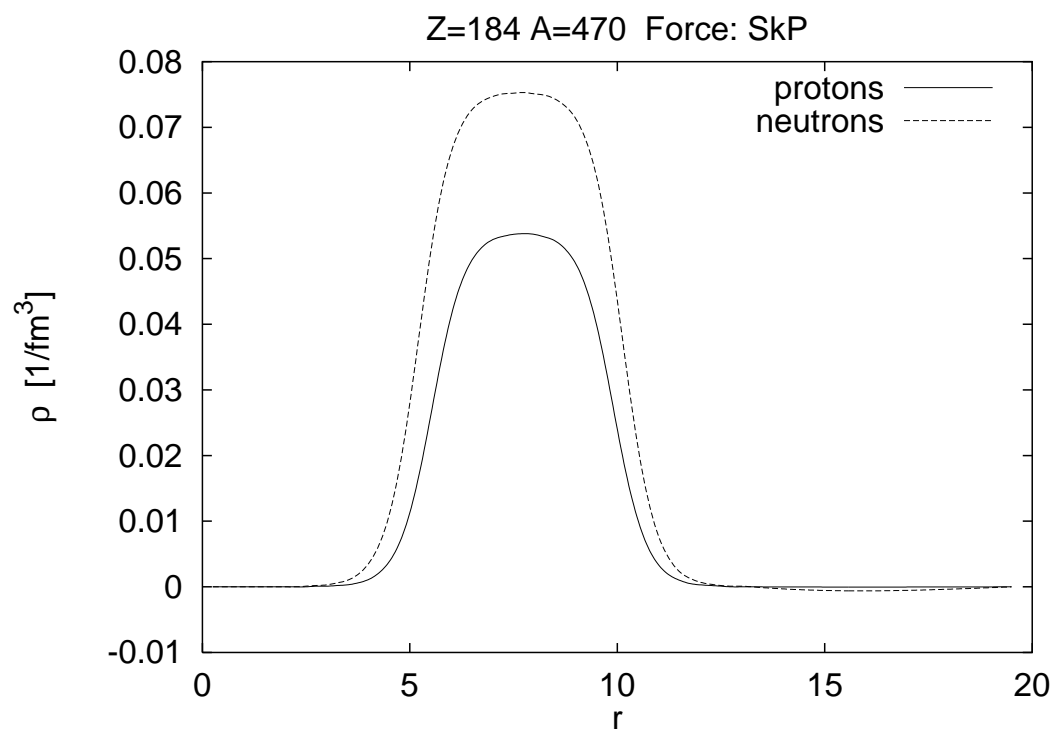Figure 1:

Figure 2:

Figure 3:

Figure 4:

Figure 5:

Figure 6:

e_ν [100/A^{2/3} MeV]

f

50

45

40

35

30

25

20

0.05   0.1   0.15   0.2   0.25   0.3

612

550

490

500

338

416

288

340

242

294

200

162

Left labels (top to bottom):
1q25/2
3i13/2
3i11/2

1q27/2
2l19/2
3h11/2
2l17/2
3h 9/2
1o23/2

3g 9/2
3g 7/2
1o25/2
2k17/2

2k15/2
3f 7/2
1n21/2
3f 5/2

3d 5/2
3d 3/2
1n23/2
3p 3/2
2j15/2
3p 1/2
2j13/2
3s 1/2
1m19/2

1m21/2
2i13/2
2i11/2

1l17/2

1l19/2
2h11/2
2h 9/2

1k15/2

1k17/2
2g 9/2

Right labels (top to bottom):
2i13/2
1t31/2
2i11/2

2h11/2
2h 9/2

1r27/2
2g 9/2
2g 7/2
1r29/2
2f 7/2
2f 5/2
2d 5/2
2d 3/2
2p 3/2
2p 1/2
2s 1/2
1q25/2

1q27/2

1o23/2
1o25/2

1n21/2
1n23/2

1m19/2
1m21/2

1l17/2
1l19/2

1k15/2
1k17/2

Figure 7:

44

Figure 8:

Figure 9:

46

y-axis: e_ν [100/A$^{2/3}$ MeV]

x-axis: f

Left-side labels (top to bottom):
2j15/2
2j13/2
3f 7/2
3f 5/2
1m21/2
1m19/2
3d 5/2
3d 3/2
2i13/2
3p 3/2
2i11/2
3p 1/2
1l19/2
3s 1/2
1l17/2
2h11/2
1k15/2
2h 9/2
1k17/2
2g 9/2
2g 7/2
1j13/2
1j15/2
2f 7/2
2f 5/2
1i11/2
1i13/2
2d 5/2
2d 3/2
2p 3/2
2p 1/2
1h 9/2
2s 1/2
1h11/2
1g 7/2
1g 9/2
1f 7/2
1f 5/2

Right-side labels (top to bottom):
2h 9/2
2g 9/2
2g 7/2
2f 7/2
1n23/2
2f 5/2
2d 5/2
1n21/2
2p 3/2
2d 3/2
2p 1/2
2s 1/2
1m21/2
1m19/2
1l19/2
1l17/2
1k17/2
1k15/2
1j15/2
1j13/2
1i13/2
1i11/2
1h11/2
1h 9/2
1g 9/2
1g 7/2
1f 7/2
1f 5/2
1d 5/2
1d 3/2
1p 3/2
1p 1/2
1s 1/2

Magic numbers in figure:
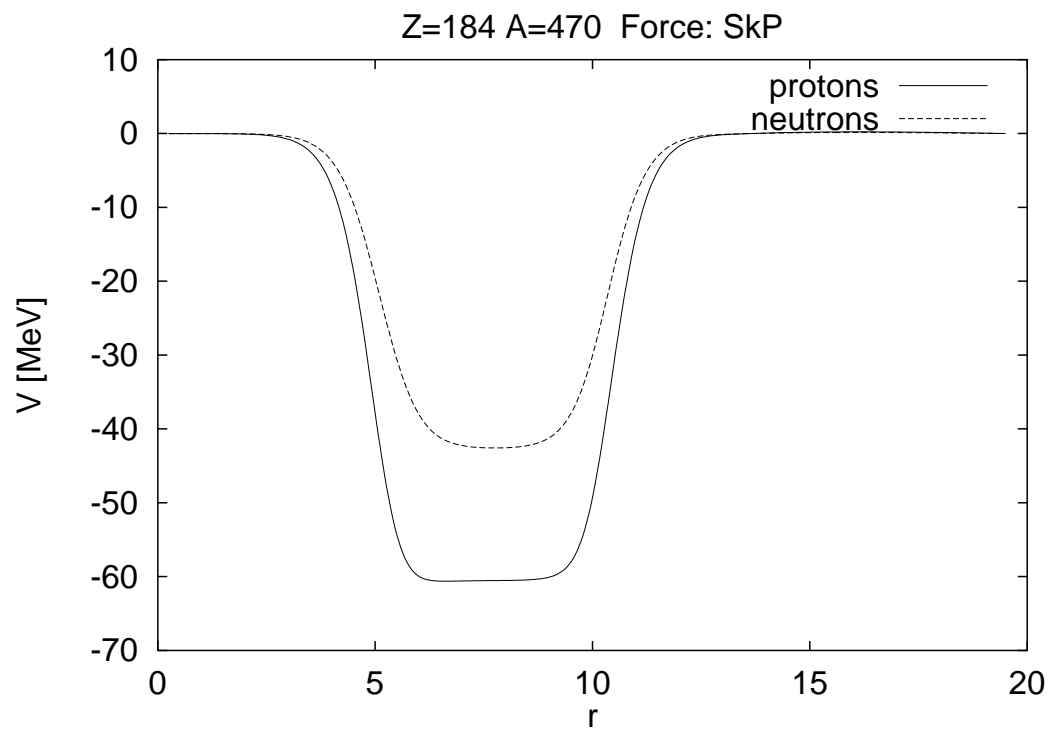372, 354, 340, 302, 284, 272, 212, 162, 128, 98, 72, 72, 50, 32

Figure 10:

Figure 11:

Figure 12:

Figure 13:

Figure 14:

Figure 15:

Figure 16:

Figure 17:

Figure 18:

Figure 19:

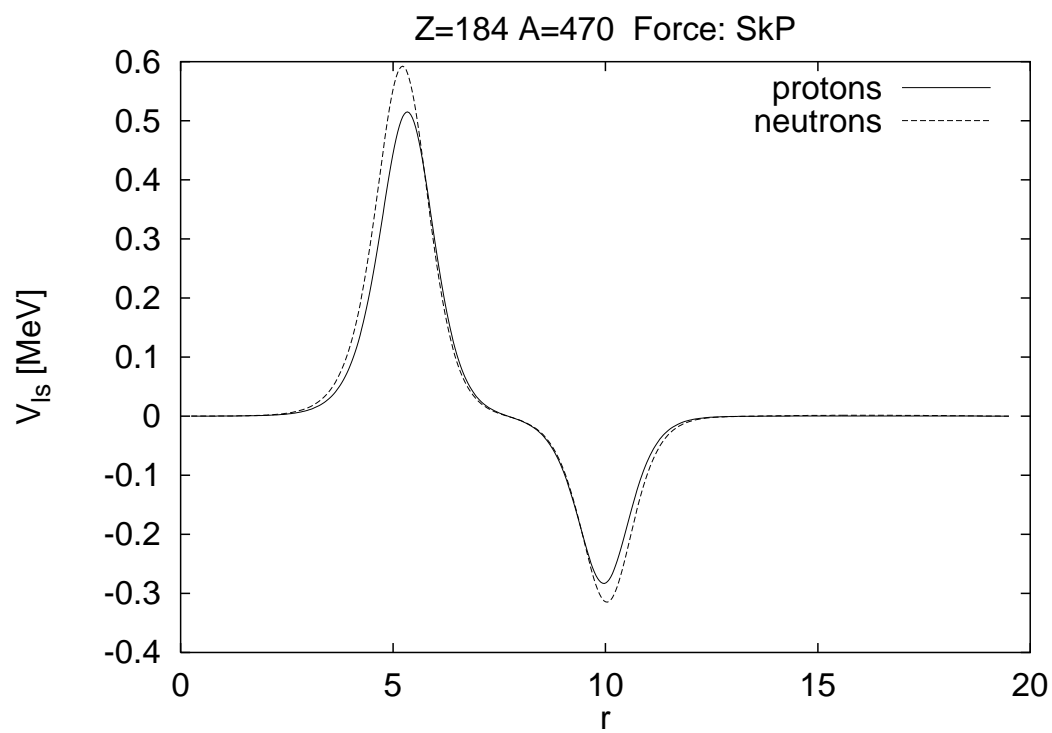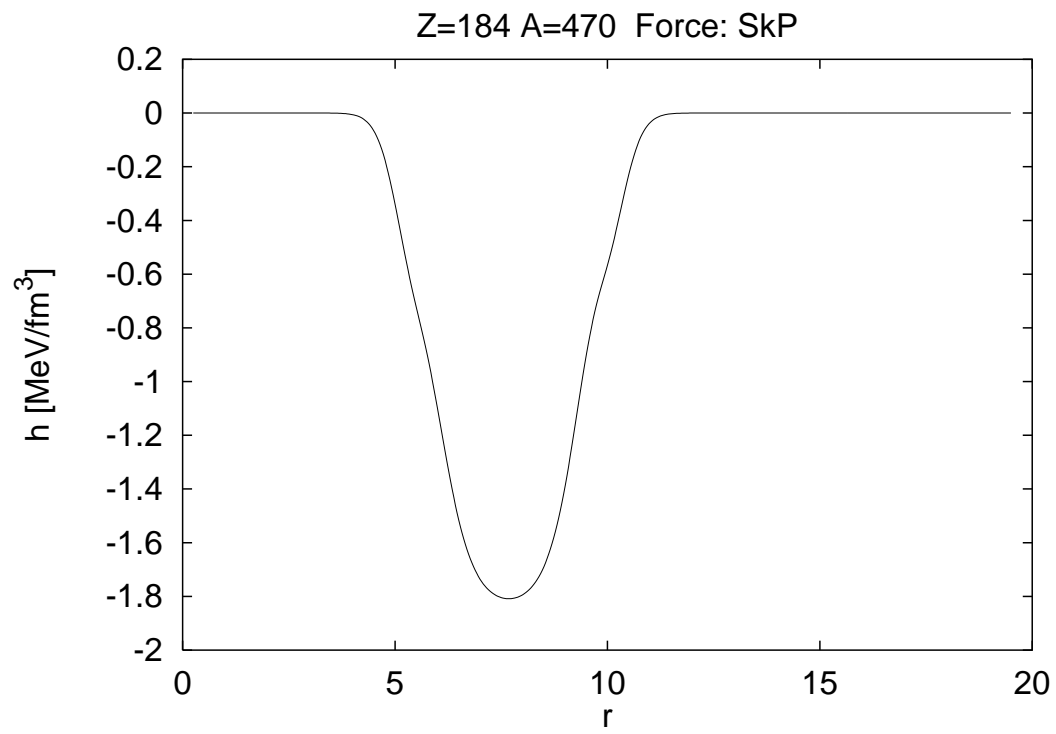Figure 20:

Figure 21:

Figure 22:

Figure 23:

Z=184 A=470 Force: SkP

Figure 24:

61

Figure 25:

Figure 26:

Figure 27: